INVESTIGATION OF THE PHOTO-RESPONSE OF GRAPHENE/SILICON PHOTODETECTOR IN THE ULTRAVIOLET REGION

A Thesis Submitted to
The Graduate School of
İzmir Institute of Technology
In Partial Fulltime of the Requirements for the Degree of

MASTER OF SCIENCE

In Physics

by
Çiçek KAPLAN

July 2024
İZMİR

We approve the thesis of **Çiçek KAPLAN**

Examining committee members:

Prof. Dr. Cem ÇELEBİ
Department of Physics, İzmir Institute of Technology

Prof. Dr. Lütfi ÖZYÜZER
Department of Physics, İzmir Institute of Technology

Assoc. Prof. Dr. Gökhan UTLU
Department of Physics, Ege University

9 July 2024

Prof. Dr. Cem ÇELEBİ
Supervisor, Department of Physics,
İzmir Institute of Technology

Asst. Prof. Dr. Özhan ÜNVERDİ
Co-Supervisor, Department of Electrical and Electronic Engineer,
Yasar University

Prof. Dr. Lütfi ÖZYÜZER
Head of the Department of Physics

Prof. Dr. Mehtap EANES
Dean of the Graduate School

ACKNOWLEDGMENTS

I would like to express my deepest gratitude to my thesis advisor Prof. Dr. Cem ÇELEBİ, for his supporting me throughout my research studies, and help in my entire learning process. Cem Çelebi's feedback helped to shape and improve this thesis. I feel fortunate to have had the opportunity to work with him, and I also offer my sincere appreciation for his outstanding guidance. I am profoundly thankful for his effect on me academically and his contribution to my development.

I would like to thank the Scientific and Technological Research Council of Turkey (TÜBİTAK) my scientific research is supported within the scope of Project NO. 122F022.

I would be grateful to all QDL member for being friendly, helping me in a laboratory working environment and always being open to sharing experimental knowledge. Additionally, I also thank my dear friends Buket Özgün, Elif Kiraz, Yılmaz Can Yüksek, Pelin Polat and Zeynep Aslı Akyürek for giving motivation and always being by my side during the thesis period.

Also, I would like to thank my dear love Emre Dinçer for his endless support and, always being there for me in my hard times.

And last but not least, I am very grateful to my dear parents and sisters always gave me their endless support, especially my mother who believed in me.

ABSTRACT

INVESTIGATION OF THE PHOTO-RESPONSE OF GRAPHENE/SILICON PHOTODETECTOR IN THE ULTRAVIOLET REGION

In this thesis, we focus on the optoelectronic properties of p-type graphene and n-type Silicon (Gr/Si) Schottky barrier photodiode according to the number of layers in the ultraviolet region (UV). The I-V measurements were conducted at an applied bias voltage between -0.5 and 0.5 V for each Gr/Si heterojunction. The I-V measurements taken under dark conditions showed that all Gr/Si samples with 2-, 4- and 6-layers graphene electrodes exhibited rectifying Schottky junction character, but all device's reverse saturation currents (I_0) were different. Schottky barrier heights (Φ_B) of the samples with 2-, 4- and 6-layers graphene electrodes were determined using the I_0 values obtained from I-V measurements. Compared to the Φ_B value of the sample with 2 layers graphene electrode, the Φ_B of the sample with 4 layers of graphene electrode increased to ~0.82 eV, and then Φ_B was found to decrease to ~0.79 eV for the 6-layer graphene electrode. Additionally, photo-response measurements were carried out at zero bias voltage and in the wavelength range of 250 – 400 nm to determine the spectral response (R) of the devices in the UV region. Compared to the device with 2 layers graphene electrode, R of the sample with 4 layers graphene electrode increased by 3 times. The result obtained revealed that using 4-layer graphene as a light-transparent electrode, Gr/Si Schottky barrier photodiode is the most applicable option for sensitive detection of light in the UV region.

ÖZET

MORÖTESİ BÖLGEDE GRAFEN/SİLİKON FOTODEDEKTÖRÜN FOTO-TEPKİSİNİN ARAŞTIRILMASI

Bu tez çalışmasında, Kimyasal Buhar Biriktirme yöntemi ile üretilen p-tipi grafen ve n-tipi Silisyum (Gr/Si) bazlı Schottky bariyer fotodiyotunun fabrikasyonu ve bu fotodiyotun morötesi bölgede optoelektronik karakteristiklerinin grafen katman sayısına bağlılığı deneysel olarak incelenmiştir. Atmosferik basınçta ölçümlerde, her bir Gr/Si hetero eklemi için -0,5 ile 0,5 V arasında uygulanan öngerilim voltajında I-V ölçümleri gerçekleştirilmiştir. Karanlık ortam koşulları altında alınan I-V ölçümleri 2, 4 ve 6 katmanlı grafen elektrota sahip Gr/Si örneklerin tamamının düzeltici (rectifying) Schottky eklem karakteri sergilediği ancak ters doyma akımlarının (I_0) farklı olduğu bulunmuştur. I-V ölçümlerinden elde edilen I_0 değerleri kullanılarak 2, 4 ve 6 katmanlı grafen elektrotlu numunelerin Schottky bariyer yükseklikleri (Φ_B) saptanmıştır. İki katmanlı grafen elektrota sahip örneğin Φ_B değerine göre 4 katman grafen elektrotlu örneğin Φ_B değeri ~0,82 eV düzeyine çıktığı ve ardından 6 katman grafen elektrodu için yaklaşık ~0,79 eV 'a düştüğü bulunmuştur. Elde ettiğimiz bu sonuçlar, Gr/Si fotodiyottaki düzeltme kuvvetinin, aygıt yapısında şeffaf iletken elektrot görevi gören grafen katmanlarının sayısı ile değiştirilebileceğini göstermektedir. Ayrıca, aygıtların morötesi bölgesindeki spektral tepkisini (R) belirlemek için sıfır ön gerilimde ve 250 – 400 nm dalga boyu aralığında foto-tepki ölçümleri gerçekleştirilmiştir. 2 katmanlı grafen elektrotlu aygıta kıyasla, 4 katmanlı grafen elektrotlu örneğin spektral duyarlığı 3 kat artmasına rağmen, 6 katmanlı grafen elektrotlu aygıtta 4 katmanlı grafen elektrotlu aygıtın spektral duyarlığına göre yaklaşık 25% azalma olduğu belirlenmiştir. Elde edilen sonuçlar, 4 katmanlı grafenin ışık geçirgen bir elektrot olarak kullanılmasının, Gr/Si Schottky bariyer fotodiyotun derin morötesi bölgede ışığın hassas olarak algılanması için en uygun seçenek olduğunu ortaya koymuştur.

To My Mother

TABLE OF CONTENTS

LIST OF FIGURES

Figures **Page**

Figures **Page**

Figures **Page**

LIST OF TABLES

Table **Page**

LIST OF SYMBOLS

C	Carbon
σ	Sigma
q	Elementary charge
n	Concentration of electrons
μ_e	Electron mobility
p	Concentration of holes
μ_h	Hole mobility
Φ_M	Work function of metal
Φ_S	Work function of the semiconductor
R_s	Series resistance
η	Ideality factor
Φ_B	Barrier height
χ	Electron affinity
V_i	Contact potential
$I_{S\rightarrow M}$	Semiconductor-to-metal current density
A*	Richardson constant
T	Temperature
k_b	Boltzmann constant
$I_{M\rightarrow S}$	Metal to the semiconductor
$E_F{}^G$	Fermi level of graphene
Ir	Iridium
Cu	Copper
H_2	Hydrogen
Ar	Argon
I_G	G Intensity of graphene on Raman
I_{2D}	2D Intensity of graphene on Raman
$FeCl_3$	Iron (III) chloride
HCl	Hydrochloric acid
HF	Hydrofluoric acid
SiO_2	Silicon oxide
Ni	Nickel

Cr	Chromium
Al	Aluminium
Au	Gold
V_0	Bias Voltage
I_0	Saturation currents
I_d	Dark currents
A	Junction area
R	Spectral response
I_p	Photocurrent
P (λ)	Incident light power
D*	Specific detectivity
t_r	Rise time
t_f	Fall time
E_f^2	Fermi level of 2 layers graphene electrode
E_f^4	Fermi level of 4 layers graphene electrode
E_f^6	Fermi level of 6 layers graphene electrode

LIST OF ABBREVIATIONS

2D	Two dimensional
Gr	Graphene
Si	Silicon
e-h	Electron-hole pairs
Gr/n-Si	Graphene/n-type silicon
UV	Ultraviolet
NIR	Near-infrared
M/S	Melal/Semiconductor
CVD	Chemical vapor deposition
PR	Photoresist
DI	Deionized water
IPA	Isopropyl alcohol
PCB	Printed circuit board
LED	Light emitting diode
TE	Thermionic Emission
NEP	Noise equivalent power
SBH	Schottky Barrier Height
QDL	Quantum Device Laboratory

CHAPTER 1

INTRODUCTION

1.1. Graphene

Graphene is a single-atom-thickness, planer layer of carbon atoms arranged in a 2-dimensional (2D) hexagonal honeycomb structure (Geim and Novoselov 2007) discovered by Geim and Novoselov in 2004 (Allen, Tung, and Kaner 2010). A carbon atom with four valence electrons contains one 2 $\hat{s}$ electron and three 2 $\hat{p}$ electrons, and 2 $\hat{s}$ electron and two 2 $\hat{p}$ electrons form sp^2 hybridization (Marconcini and Macucci 2007; Reina et al. 2008). It forms strong sigma (σ) bonds between carbon atoms, leading to a hexagonal structure with a carbon-carbon distance of 0.142 nm (Allen, Tung, and Kaner 2010). The 2 $\hat{p}$ electrons remaining without bonding occur as a $2\hat{p}_z$ orbital oriented perpendicular to the planar structure and form a π -bond with neighbouring carbon atoms (Wright, Liu, and Zhang 2009; Suzuki, Tanabe, and Fujita 2017; Raj and Eapen 2019). The π -orbitals give rise to weak van der Waals forces (De Andres, Ramírez, and Vergés 2008). Figure 1.1 shows the geometric and atomic structure of graphene. Figure 1.1 (a) shows carbon atoms in two different sublattices. These two different carbon atoms are called A and B as black and white circles, respectively (Dash, Pattanaik, and Behera 2014). The shaded area represents the unit cell. Shows that sp^2 hybridization orbitals between carbon atoms in Figure 1.1 (b). Here, the three nearest neighbour carbon atoms distributed symmetrically form a sigma (σ) bond (Zhang et al. 2011). The remaining electrons are shown in Figure 1.1 (c), and they are distributed perpendicular to the plane. Each carbon atom assigned four bonds' forms π bonds with the orbital of its nearest neighbour. The arrangement of carbon atoms in the A and B lattice area in two different orientations, and the hexagonal structure of the A and B carbon atoms as two intertwined triangular lattices as seen in Figure 1.1 (d). Sigma electrons give rise to energy bands far from the Fermi level (Dash, Pattanaik, and Behera 2014).

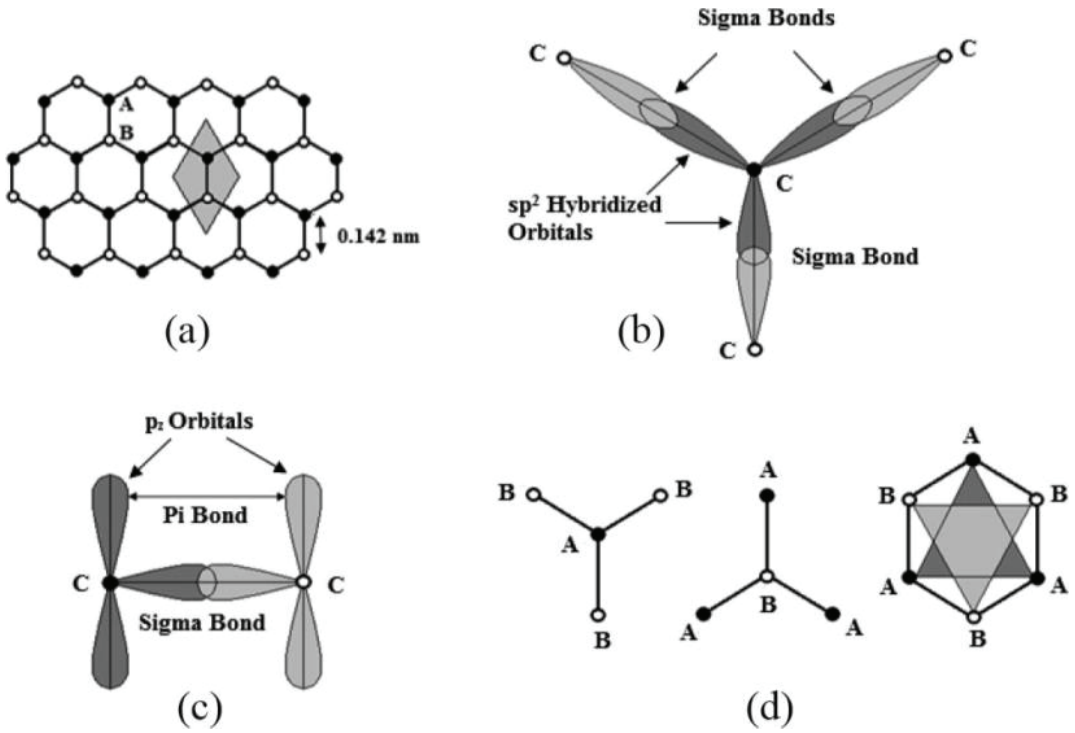

Figure1.1. (a)Two different carbon atoms called A and B in the hexagonal structure, the shaded region shows the primitive unit cell, (b) sp2 hybridization forming 1200, (c) Out-of-plane bond formation and (d) Orientation of two different carbon atoms.(Dash, Pattanaik, and Behera 2014)

The hexagonal Bravais lattice of graphene (Gupta, Sakthivel, and Seal 2015; Di Bartolomeo 2016) forms the smallest repeating structure called a unit cell. The crystal structure of graphene based on two atoms can appear as a triangular Bravais lattice as shown in Figure 1.2 (a) (Castro Neto et al. 2009). The lattice vectors are a_1 and a_2 (Marconcini and Macucci 2007) can be written as:

$$\overrightarrow{a_1} = a\left(\frac{3}{2}, \frac{\sqrt{3}}{2}\right) \quad , \quad \overrightarrow{a_2} = a\left(\frac{1}{2}, \frac{-\sqrt{3}}{2}\right) \qquad (1.1)$$

The reciprocal lattice vectors b_1 and b_2 can be written as follows;

$$\overrightarrow{b_1} = \frac{2\pi}{a}\left(\frac{1}{2}, \frac{\sqrt{3}}{2}\right) \quad , \quad \overrightarrow{b_2} = \frac{2\pi}{a}\left(\frac{1}{2}, \frac{-\sqrt{3}}{2}\right) \qquad (1.2)$$

The Graphene Brillouin zone is a parallel formed in the reciprocal space of the initial Bravais lattice of a crystal shown the Figure 1.2 (b). It also represents the place of wave vectors in the carbon crystal structure. The zone centre and midpoint are defined Γ and M, respectively (Wright, Liu, and Zhang 2009). As seen in Figure 1.2 (c), the conduction band and valence band of graphene touch each other at six points in reciprocal space. The contact by the conduction and valence bands is called the Dirac point. The two equivalents K and K' at the corner of the hexagonal Brillouin zone (Marconcini and Macucci 2007) are defined as:

$$\vec{K} = \frac{2\pi}{3a}\left(1, \frac{1}{\sqrt{3}}\right) \quad , \quad \overrightarrow{K'} = \frac{2\pi}{3a}\left(1, \frac{1}{\sqrt{3}}\right) \qquad (1.3)$$

The Fermi level of intrinsic graphene is exactly in the middle point. The electron distribution (k) around the Dirac points of graphene is linear (Giubileo and Di Bartolomeo 2017). This indicates that graphene due to linear distribution behaves like relativistic and massless particles (fermions) (Novoselov et al. 2005). Charge carriers close to the Dirac points move with Fermi velocity (v_f = 10^6 m/s) (Giubileo and Di Bartolomeo 2017; Suzuki, Tanabe, and Fujita 2017).

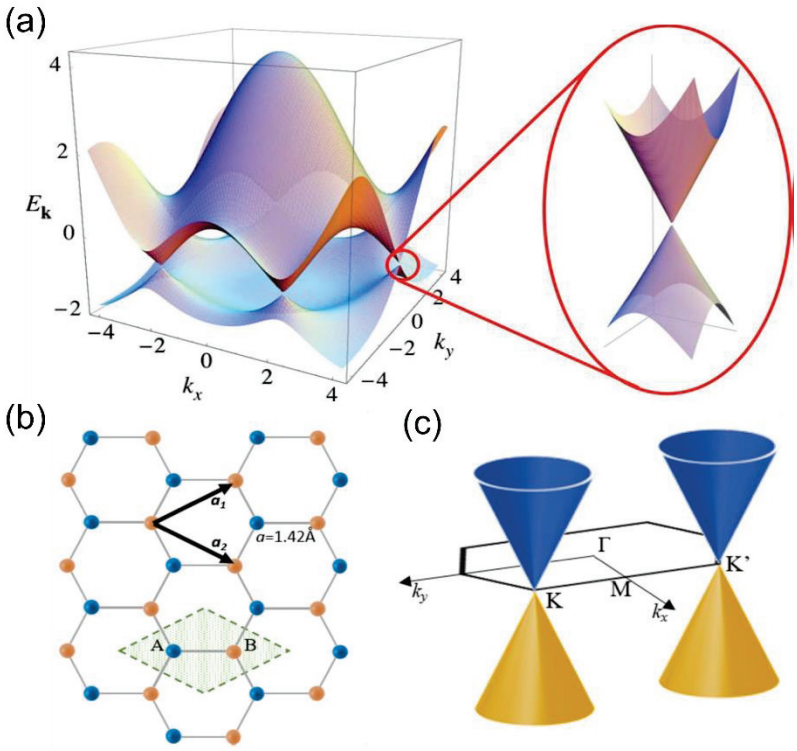

Figure 1.2. (a) First Brillouin zone and band structure of graphene. (b) Real-space lattice with primitive and the nearest neighbour vectors and (c) K is the corner of the zone and Γ is the zone centre. M is the midpoint between adjacent non-equivalent corners in the reciprocal space. (Castro Neto et al. 2009; Giubileo and Di Bartolomeo 2017)

The electrical conductivity (σ) of graphene is calculated by $\sigma = e\,(n\mu_e + p\mu_h)$, where e is the elementary charge, n is the concentration of electrons, μ_e is the electron mobility, p is the concentration of holes and μ_h is the hole mobility (Marconcini and Macucci 2007; Morozov et al. 2008; Yang and Murali 2011). The theoretical limit of graphene's carrier mobility is approximately 2×10^5 $cm^2/V{\cdot}s$ at the carrier density on the order of a few 10^{12} cm^{-2} at room temperature (Novoselov et al. 2012; Morozov et al. 2008). Depending on the doping type, the Fermi level of graphene shifted upward (n-type) or downward (p-type) relative to the Dirac point (Di Bartolomeo 2016). The linear distribution with conduction and valence bands along the Dirac point is shown in Figure 1.3. It is also called the Dirac cone. During the charge transfer from graphene, it leads to electron or hole contribution, which provides a transition above or below the Dirac point of the Fermi Level (E_f).

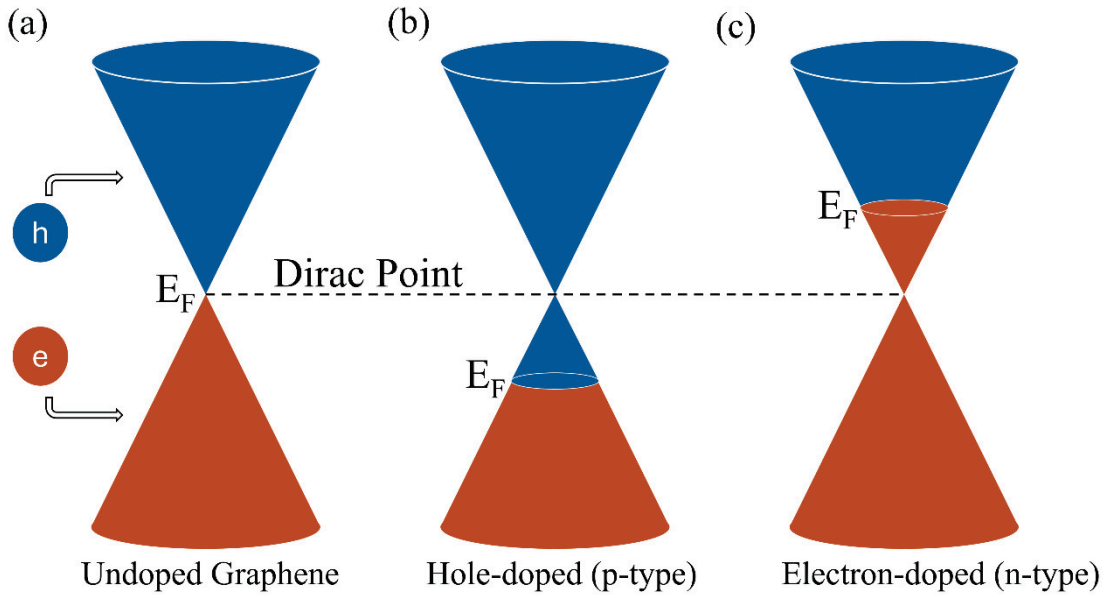

Figure 1.3. The bond structure of (a) undoped or intrinsic (b) hole doped (c) electron doped graphene.

1.2. Schottky Junction Mechanism

Schottky Junction first discovered in the 1960s that the metal/semiconductor (M/S) contact creates a potential barrier relative to other diodes. In this model, the electric field formed in the semiconductor increases linearly and the potential decreases as it moves away from the depletion region, according to Gauss' law (Zeghdar et al. 2015). This M/S heterojunction structure is called the Schottky diode. Unlike conventional p-n or p-i-n junction diodes, Schottky Diodes are formed using a metal electrode connected to a n-type semiconductor. Metal contact is usually made of highly conductive metals for instance Platinum (Pt), Gold (Au), and Silver (Ag). The schematic structure and symbol of the Schottky diode are shown in Figure 1.4.

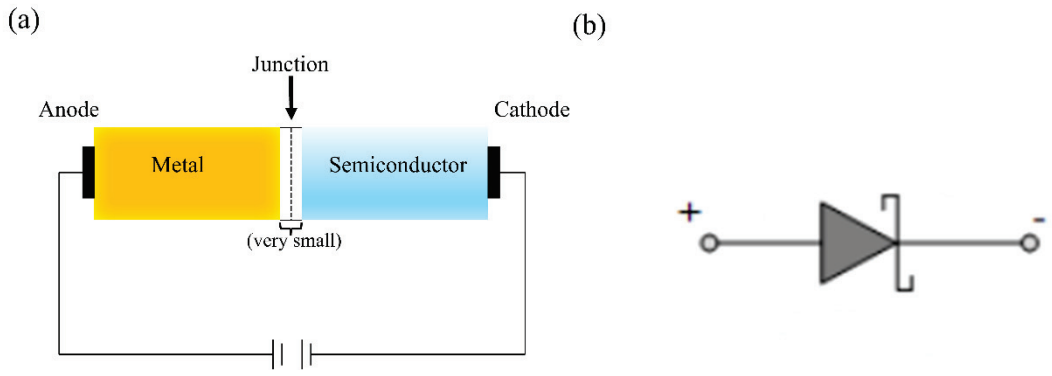

Figure 1.4. (a) Conventional metal-semiconductor Schottky junction, and (b) its circuit

M/S heterostructures are defined in two different ways rectifier and ohmic contact. In the rectification contact, electron-hole (e-h) pairs which are the charge carriers that provide conductivity, enable an electric current to be transmitted to the other direction more easily. If it is in ohmic contact, carriers can be easily transmitted in all directions (Xu et al. 2016). Table 1.1 shows the rectification and ohmic contact table according to the work function (Φ_M).

Table 1.1. Rectification and ohmic contact type according to the work function

.

Work Function	Type of Semiconductor	Type of Contact
$\Phi_M > \Phi_S$	n- type	Rectification
$\Phi_M < \Phi_S$	n-type	Ohmic
$\Phi_M > \Phi_S$	p-type	Ohmic
$\Phi_M < \Phi_S$	p-type	Rectification

Each metal has its unique Φ_M. A potential barrier is formed by the difference between the Φ_M of the metal and Φ_S of the semiconductor (Tongay et al. 2011). M/S Schottky diodes have fundamental parameters such as series resistance (R_s), ideality factor (η) and barrier height (Φ_B). Thermionic emission (TE) theory is used to explain the temperature dependent Schottky barrier diode current conduction mechanism and to obtain its physical parameters (Zeghdar et al. 2015).

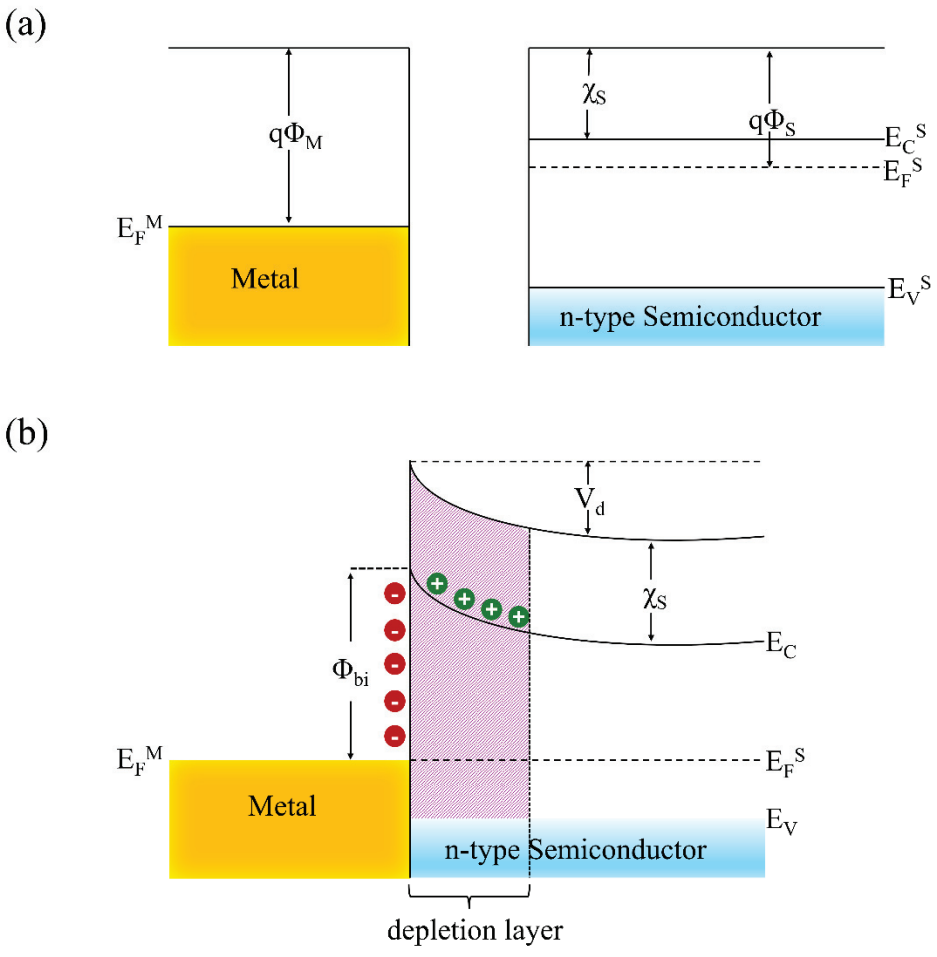

Figure 1.5. Energy band diagram of the M/S junction (a) before contact and (b) after contacting thermal equilibrium conditions.

Figure 1.5 shows the energy band diagrams of M/S contacts. Figure 1.5. (a) represents the before-connection, and Figure 1.5. (b) represents the after-connection under the thermal equilibrium. Here, the work function of the metal is given by $q\Phi_m$, and the work function of the semiconductor is given by $q\chi$-$q\Phi_s$, where $q\chi$ is the electron affinity and $q\Phi_{bi}$ is the difference in energy between the conduction band and the Fermi level. The difference between these two equations allows us to find the contact potential (qV_i) (S. S. Li 1993). The barrier height of the electron moving from the metal to the semiconductor is defined as follows:

$$q\Phi_B = q(\Phi_M - \chi) \qquad (1.4)$$

The applied forward or reverse bias voltage changes the energy-band diagram in thermal equilibrium. This change is resulting in the potential and band in the depletion region to bend.

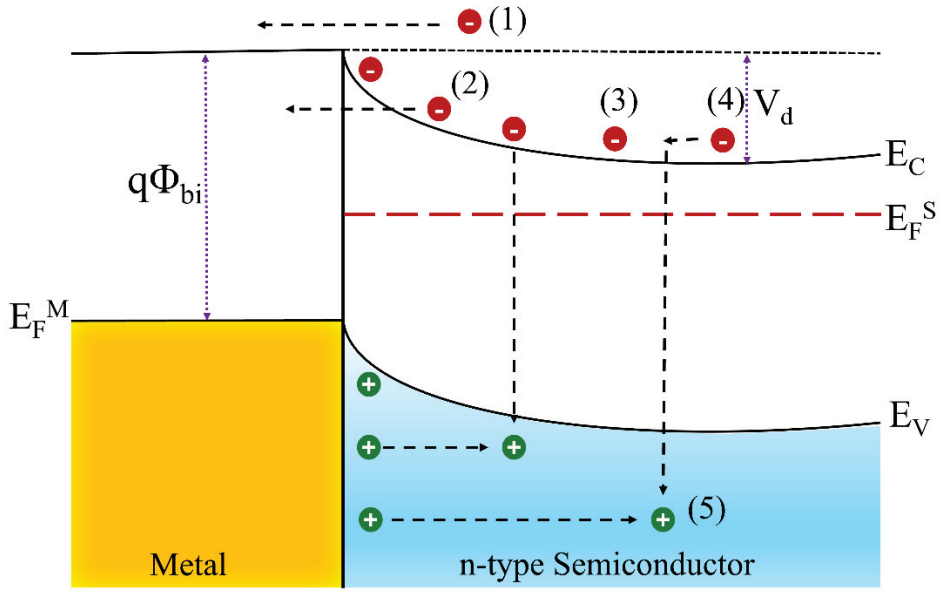

Figure 1.6. Schottky Junction charge flow mechanisms under forward bias.

Figure 1.6. defines that (1) charge transitions from the barrier by TE, (2) quantum tunnelling across the barrier, (3) recombination in the depletion region, and (4) (5) the diffusion of carriers across the depletion region. The effect of the charge flow is due to TE at room temperature.

The definition of the semiconductor-to-metal current density $I_{S\rightarrow M}$ can be written as (Cheung and Cheung 1986):

$$I_{S\rightarrow M} = \int_{E_f+q\Phi_B}^{\infty} q\vartheta_x dn \qquad (1.5)$$

$$I_{S\rightarrow M} = A^* T^2 (\frac{-q\Phi_B}{k_B T}) exp(\frac{qV}{k_B T}) \qquad (1.6)$$

where (A*) is the Richardson constant, (T) temperature, (k) Boltzmann constant. The total current density flowing from the metal to the semiconductor $I_{M\rightarrow S}$ can be written as (Cheung and Cheung 1986):

$$I_{M\rightarrow S} = A^* T^2 exp\left(\frac{-q\Phi_B}{k_B T}\right)\left[\exp\left(\frac{qV}{\eta k_B T}\right) - 1\right] \quad (1.7)$$

$$I_{M\rightarrow S} = A^* T^2 exp\left(\frac{-q\Phi_B}{k_B T}\right) \quad (1.8)$$

1.3.p-type Gr/n-type Si-Based UV Schottky Photodiode

The Graphene/Silicon (Gr/Si)-based heterojunction photodiode is generally created by transferring graphene to the silicon surface (Di Bartolomeo et al. 2018; Wang et al. 2020). Recently, Gr/Si-based heterojunction has been widely used in ultraviolet, visible, and near-infrared (NIR) application sensors technologies (Lv et al. 2013; Pelella et al. 2021) due to the unique features such as electronic, optical, and mechanical properties of graphene (Periyanagounder et al. 2018; Pang et al. 2011).

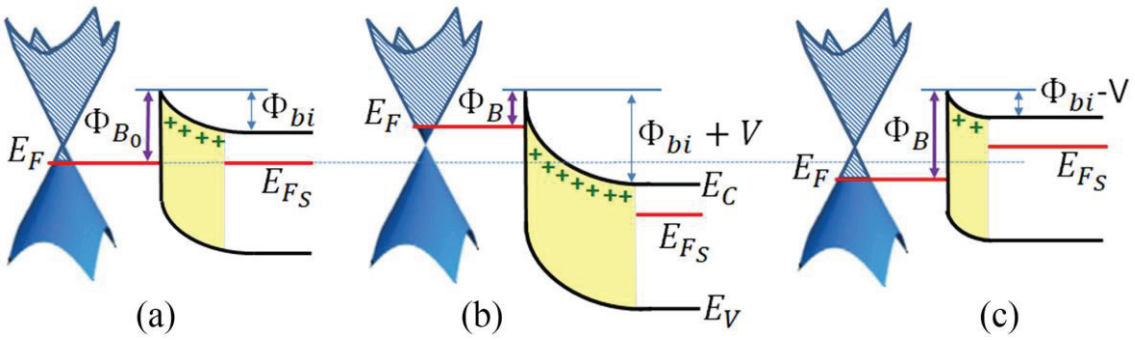

Figure 1.7. Energy band diagram of Graphene/Semiconductor heterojunction (a) under the thermal equilibrium (b) forward bias and (c) reverse bias condition. (Di Bartolomeo et al. 2018)

Gr/Si-based heterojunction exhibits rectifying current-voltage (I-V) properties as a result of the formation of the Schottky barrier, similar to conventional M/S Schottky diodes (Y. Kim et al. 2016; H. Y. Kim et al. 2013). Additionally, the Gr/Si-based heterojunction has features not found in M/S diodes (Xu et al. 2016; H. Y. Kim et al. 2013). The density of states at the Dirac point of graphene makes it possible to setting the Fermi level (Bartolomeo 2020). Therefore, this enables modulation of the Schottky barrier height with a single anode-cathode bias (Xinming Li et al. 2016). In addition, Gr/Si-based heterostructure photodiodes also serve as active materials for graphene light absorption and electron-hole generation and separation (Ponraj et al. 2016). The energy band diagrams of the Gr/Si-based heterojunction are given in Figure 1.7. Figure 1.7 (a) under the zero bias, the Fermi level is at the Dirac point and the interface between graphene and a semiconductor. In Figure (b), applied the forward bias, the Fermi level of graphene (E_F^G) shifts downward because less charge is needed to conduct the positive charges formed in the depletion layer of the semiconductor. However, in Figure (c), if a reverse bias applied, the depletion layer is larger and the number of negative charges in graphene increases, for this reason, the E_F^G shifts upward. In this way, the Schottky barrier height (SBH) is modified (Mehmet Fidan, Ünverdi, and Çelebi 2022; Di Bartolomeo 2016).

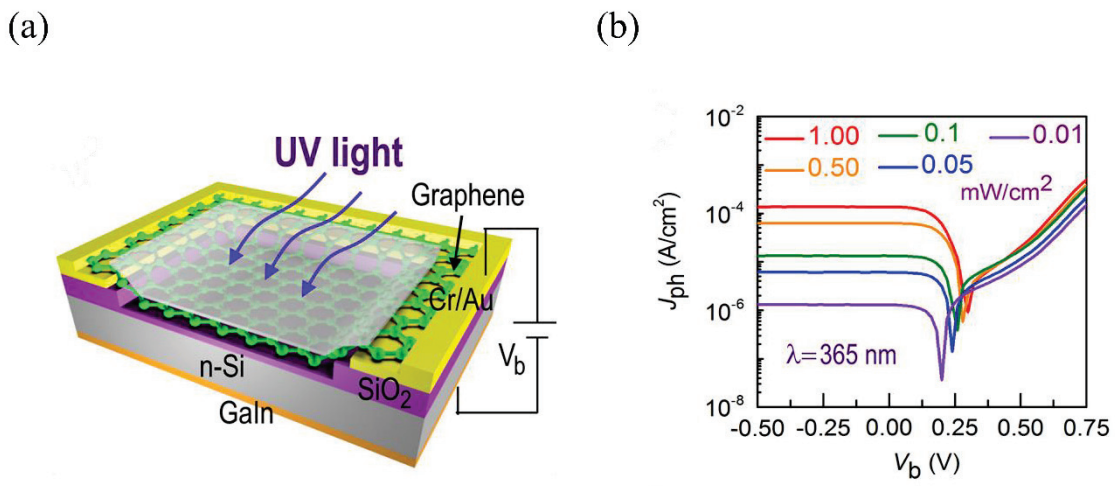

Figure 1.8. (a) Gr/Si-based photodiode and (b) semilogarithmic scale I-V curve under UV light illumination with different powers.(Wan et al. 2017)

Gr/Si photodetectors sensitive to ultraviolet (UV) light can operate in the range wavelength between 200 nm and 400 nm. Gr/Si-based Schottky photodetectors enable the detection of UV light by producing photocurrent when exposed to UV light (Wan et al. 2017). The characteristics of graphene such as its high conductivity, broad spectral response, and high carrier mobility can improve the performance of Gr/Si photodetectors (Pang et al. 2011; Bonaccorso et al. 2010). Graphene can increase the sensitivity and response time of the detector by enhanced high light absorption and fast electron transport (Nair et al. 2008). Therefore, these highly sensitive detectors respond quickly and sensitively when exposed to UV light illumination. UV Gr/Si photodetectors can be applied in many different fields due to their cheap and easy manufacturing. For example, they can be used in solar radiation monitoring, UV spectroscopy and chemical analysis fields. The development and optimization of these detectors can provide a significant technological advance for many industrial and scientific applications where UV light must be detected.

In this thesis work, we focused on the dependence of the optoelectronic characteristics of a Gr/Si-based Schottky barrier photodiode in the ultraviolet region on the number of graphene layers. The I-V measurements taken at atmospheric pressure and under dark conditions showed that all Gr/Si samples with 2, 4 and 6 layers of graphene electrodes exhibited rectifying Schottky junction character, on the other hand all device's reverse saturation currents were found to be different. The Φ_B of the samples with 2-, 4-

and 6-layers graphene electrodes were extracted from reverse saturation current values. The optoelectronic measurements were carried out at zero bias voltage and in the wavelength range of 250 – 400 nm to determine the spectral response of the devices in the UV region. In addition, time-dependent photocurrent spectroscopy measurements were done on under all devices using a 280 nm LED light source at 5 kHz frequency. Our measurements which give us on information about graphene layer electrode is the most apposite option for the sensitive detection of light in the deep UV region.

CHAPTER 2

Experimental Details

2.1. Growth of Graphene by Chemical Vapor Deposition Technique

Chemical vapor deposition (CVD) technique is a type of vapor phase transport process, in which atoms, molecules, or their mixtures of are deposited on the surface. High-quality thin films can be produced under a vacuum or atmosphere with CVD. The CVD method is most commonly used in semiconductor technology to produce thin films (Pang et al. 2011). In particular, carbon-based materials such as nanofibers, nanotubes, diamonds and graphene are produced by this method (Muñoz and Gómez-Aleixandre 2013). Using the CVD method, graphene production can be achieved at different temperatures (between 800 ^{o}C-1000 ^{o}C) on transition metals such as nickel (Ni)[69], iridium (Ir)[77] and copper (Cu)[68] (Xuesong Li et al. 2009), by means of the carbon source gas (such as CH_4, C_2H_6) sent into the furnace (Jehad et al. 2023; Suk et al. 2013).

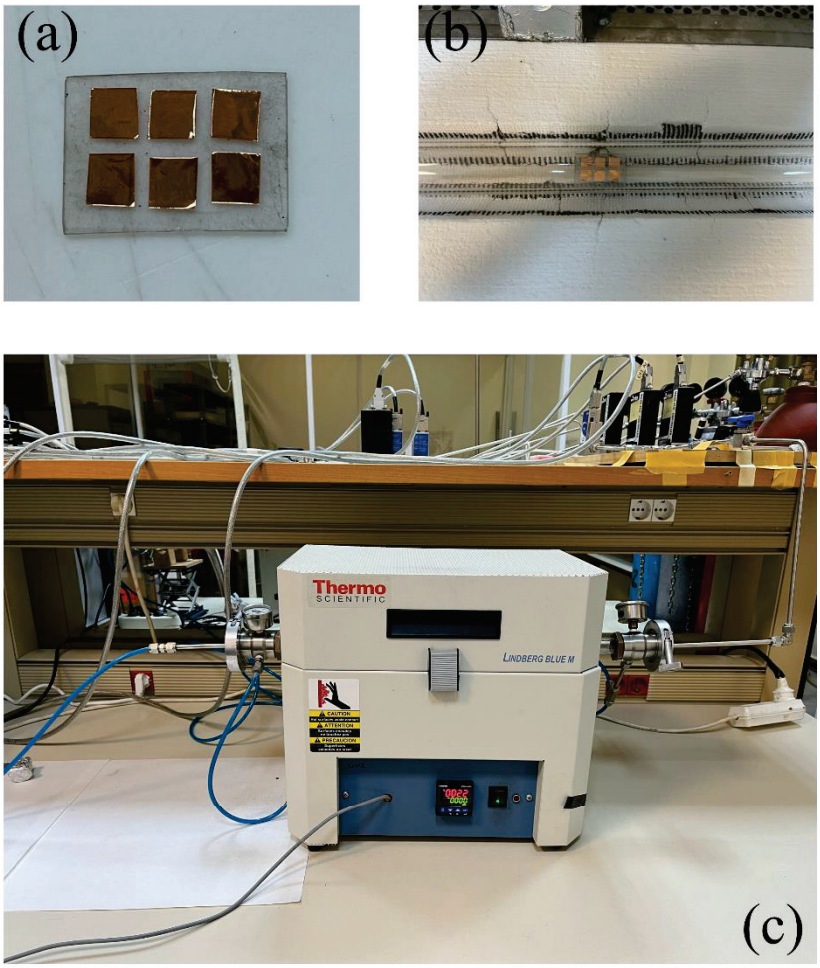

Figure 2. 1. (a) Cu foil pieces, (b) Cu foils on quartz in the middle of the furnace, and (c) CVD furnace in our laboratory.

First, a suitable substrate for graphene growth must be prepared. For this reason, 5 mm x 5 mm Cu pieces are cut cleaned and placed inside the quartz tube. The growth of graphene is done in 4 steps listed below;

1. **Heating:** The quartz tube is pumped with the help of a rough pump. Under the atmosphere, Cu foils are slowly heated to processing temperature to prevent possible thermal stress.
2. **Annealing:** The first chemical reaction occurs in this step. Here, the Cu surface is cleaned with 20 (sccm) hydrogen (H_2) and 1200 (sccm) argon (Ar) gases at high temperature (e.g. 1000 ^oC) and the surface morphology is changed.
3. **Growth:** In the catalyst substrate C atoms are arranged as graphene sheets.

4. **Cooling:** Following the graphene growth step the furnace cools down under atmospheric pressure. To prevent the reaction of graphene with oxygen-containing groups, the temperature of the furnace is adjusted to drop approximately by 200^0C under H_2 and Ar gases. The furnace is opened at 120 ^{o}C under atmospheric pressure.

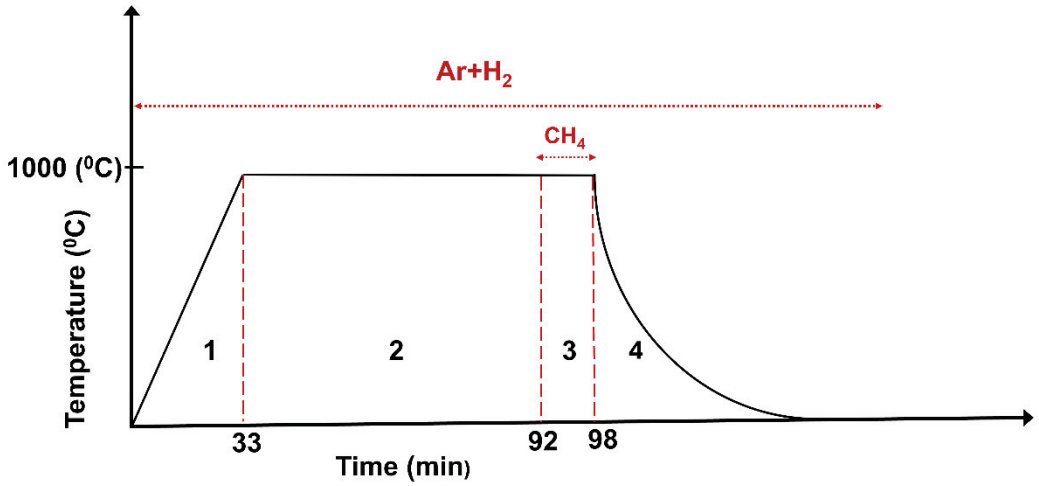

Figure 2.2. Heating (1), annealing (2), growth (3) and cooling (4) stages of graphene growth process on Cu foil with schematic representations by CVD.

In Figure 2.2, heating (1), annealing (2), growth (3) and cooling (4) steps of graphene growth on Cu foil are given with schematic representations. Cu (25 μm thick, 99.8 % purity, Alfa Aesar) pieces on the quartz plate was placed into a tube furnace (Lindberg/Blue TF55035C Split Mini Tube) as a catalyst-substrate material. During the process, a mixture of H_2 and Ar gasses were sent to the tube at 1000 ^{o}C to remove natural oxide layer on the Cu foils and to create (111) oriented grains. In the first step, the temperature is increased from room temperature to 1000 ^{o}C in 33 minutes ramp time. The reason for the slow ramp is to avoid thermal stress. Then, the Cu foil was annealed for 59 minutes under the same temperature and gas flow rates to increase the grain size of the Cu foil. For the growth phase, CH_4 gas was introduced into the tube furnace for 6 minutes to grow bilayer graphene. Finally, the sample was exposed to H_2 and Ar gases for rapid cooling from the growth temperature to room temperature. During the rapid cooling, the door of the oven was opened step by step at 800 ^{o}C, 600 ^{o}C and 400 ^{o}C, respectively.

Finally, the samples were taken out of the oven at about 140 ^{o}C. All the parameters used in the growth process are shown in Table 2.1.

Table 2.1. Growth parameters for bilayer graphene.

Temp.(C^0)	H_2 (sccm)	Ar (sccm)	CH_4 (sccm)	RT (min)	AT (min)	GT (min)
1000	20	1200	12	33	59	6

2.2. Raman Spectroscopy Measurements

Raman spectroscopy is an analysis technique based on the examination of Raman scattering resulting from the interaction of a molecule or material with light. This technique provides information about the molecular vibration and rotation modes and is used to determine the chemical composition, structure, and physical properties of a material. Raman scattering using laser light occurs when monochromatic (single wavelength) light strikes a sample and interacts with molecules (Malard et al. 2009). As a result of interaction with light, most molecules emit scattered light of the same wavelength (this is called Rayleigh scattering), but some emit different wavelengths. This difference is due to changes in the vibrational or rotational energy levels of the molecules. This causes Raman scattering.

Raman scattering patterns are analysed based on changes in wavelengths. These patterns consist of characteristic peaks that are specifically associated with the vibration and rotation modes of the molecules. These peaks provide information about a molecule's chemical structure and binding pattern. Graphene is a material that can be analysed in detail with Raman spectroscopy (Fates, Bouridah, and Raskin 2019). Raman spectrum of graphene contributes greatly to understanding the structure and characteristic properties of graphene. According to the literature, graphene has two different photon modes.

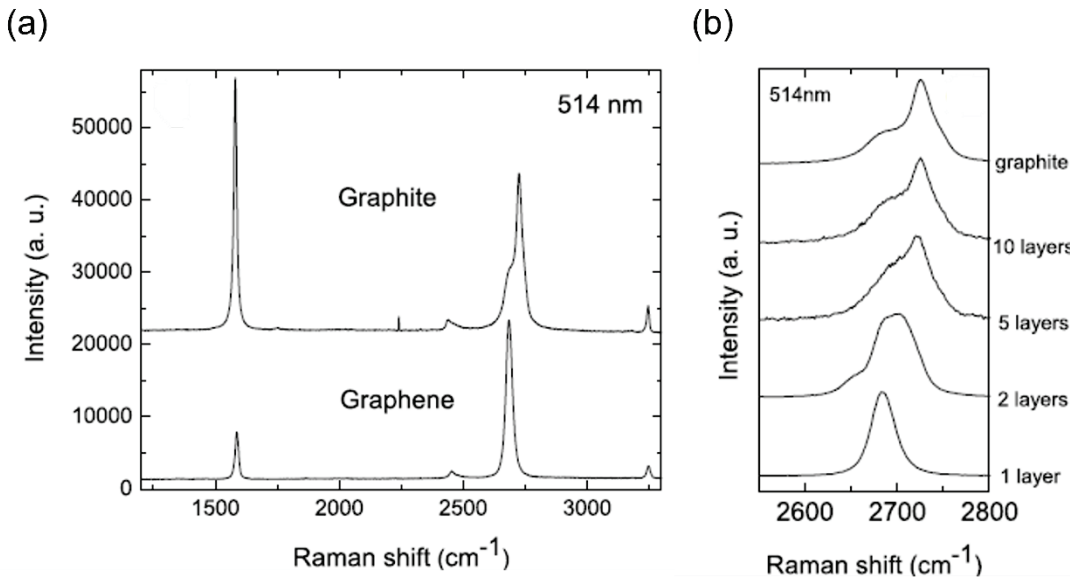

Figure 2.3. Comparison of Raman spectra at 514 nm excitation wavelength for bulk graphite and graphene. They are scaled to have a similar height to the 2D peak at 2700 cm^{-1}. (b) Evolution of the 2D peak, with the number of graphene layers. (Ferrari et al. 2006)

The Raman spectrum of graphene consists of two main bands called G-band and 2D-band peaks. The G band corresponds to the bending vibration of graphene, and the 2D band corresponds to the second-order optical mode of a graphene layer. For the graphene layer, the disorder (D) peak, G peak and 2D peak are resolved at wavenumbers of 1350 cm^{-1}, 1580 cm^{-1} and 2700 cm^{-1}, respectively. The number of graphene layers is determined by the I_G/I_{2D} ratio. If the I_G/I_{2D} ratio corresponds to 1/2, graphene is single layer, if the I_G/I_{2D} ratio equals 1, graphene is bilayer. If the I_G/I_{2D} ratio is greater than 1, graphene is either few-layer or multilayer. Additionally, the I_D/I_G ratio of graphene provides information about the number of defects. The ideal ratio of I_D/I_G is between 0.025 and 0.3. A comparison of Raman spectra at 514 nm for graphite and graphene is shown in figure 2.3. (Ferrari et al. 2006).These are peaks scaled to have a height similar to the 2D peak at 2700 cm^{-1}.

Figure 2.4. Renishaw in Via Qontor Raman Microscope in Materials Research Centre (MRC) at Izmir Institute of Technology.

To determine the number of graphene layers, Raman spectroscopy measurement was done in Material Research Centre (MRC), using the Renishaw in Via Qontor Raman microscope shown in Figure 2.4.

2.3. Thermal Evaporator System

Thermal evaporation is a method used for thin film deposition in which the source material under vacuum is evaporated high temperatures. The solid rod or pellet material used in this method is exposed to a large direct current (DC) to reach the required high melting points (Bashir et al. 2020). The thermal evaporator system used for the experiments is shown in Figure 2.5.

Figure 2.5. Nanovak NVTH-350 Thermal Evaporation System including Edwards. RV8 Turbomolecular Pump, Inficon VG401 Pressure Gauge, Ordel PC771 Temperature Gauge, SQM-160 Rate/Thickness Monitor, Pot Switch, 12V - 200A Sequential/Co-evaporation Thermal Evaporation Sources, Diener Electronic SS 304 Vacuum Chamber and CW-5000 Industrial Chiller in QDL.

Figure 2.6 (a) shows the inside of the thermal evaporator system. The baskets can be filled with chromium (Cr), silicon oxide (SiO_2), nickel (Ni) or aluminium (Al) and gold (Au). Before loading into the thermal evaporator system, the samples are cleaned with acetone, IPA, and DI during sonication for about 5 minutes, and the native oxide layer on the silicon layer was removed with HF solution. The holder placed inside, and the masks used are seen in Figure 2.6 (b). In the system, 450 nm thick SiO_2 coating was done on Si substrate at a vacuum level of 10^{-7} mbar. Then, the mask was changed and for

the contacts Cr (5 nm) then the Au (80 nm) were deposited onto SiO_2/Si substrate. Figure 2.6 (c) is the final version of the sample after thermal deposition processes.

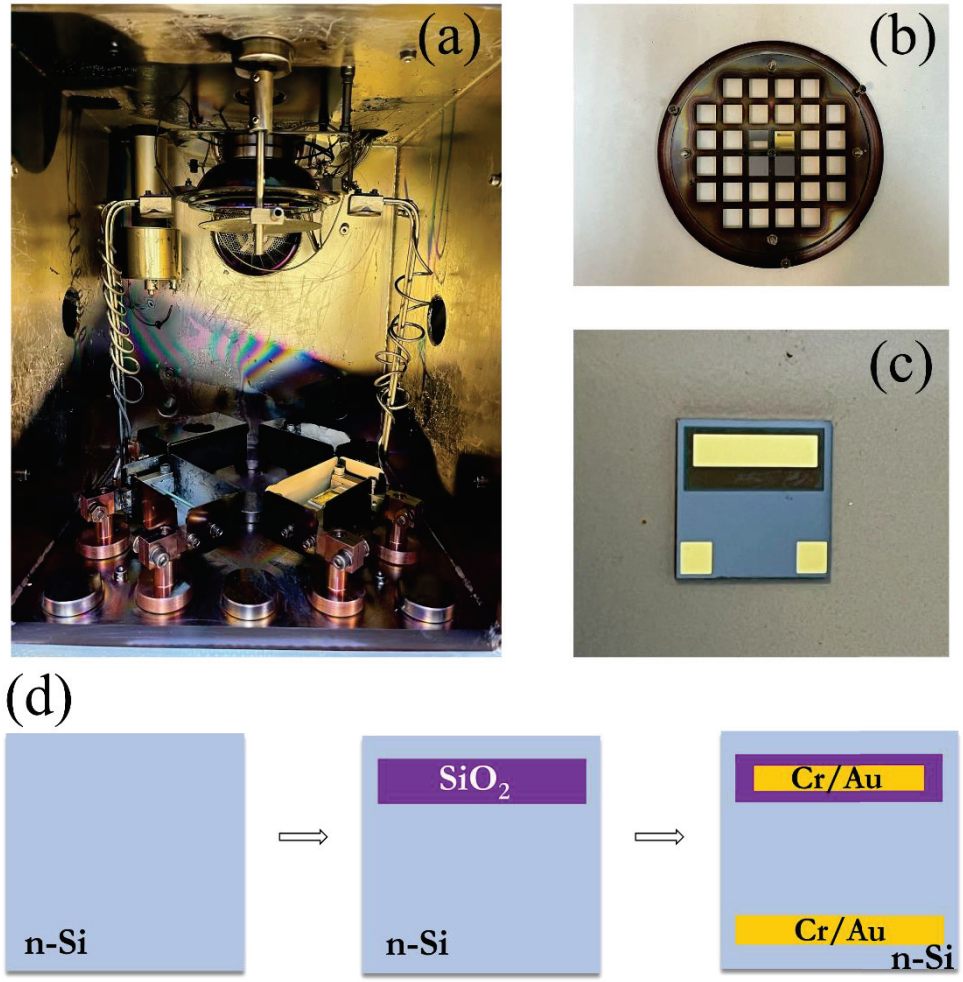

Figure 2.6. (a) Inside of the thermal evaporator system, (b) the sample holder and hard steel masks used for SiO_2 and Cr/Au deposition and (c) the final stage of the Si substrate after deposition (d) a schematic representation of the deposition process on n-Si substrate. The size of n-Si substrate is 10 mm x 10 mm.

2.4. Transfer of Graphene onto the Si Substrate

Graphene transfer steps can be seen in Figure 2.7. During the first step of the graphene transfer process, Microposit S1318 Photoresist (PR) was used to support the

graphene layer which was taken out from the CVD oven. PR was dropped onto graphene/Cu (Gr/Cu) using a micropipette and then baked in a furnace at 70 °C overnight.

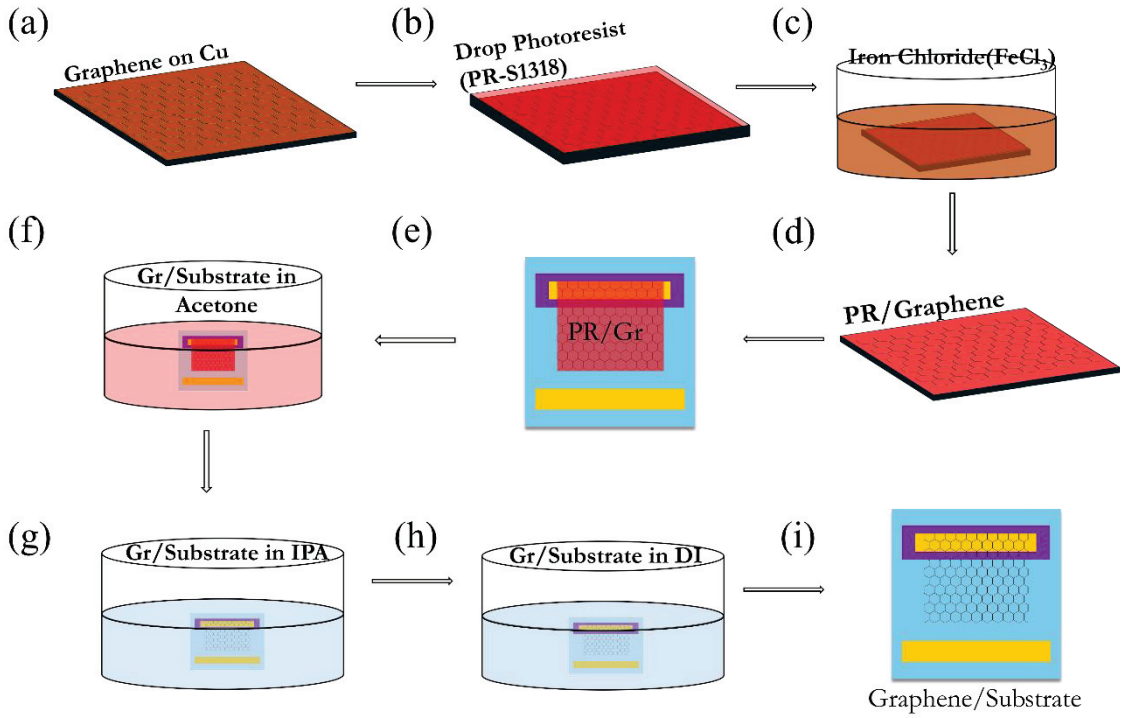

Figure 2.7. Schematic representation of the graphene transfer on Si substrate.

To etch and remove the Cu foil underneath PR/Gr stack, the sample were kept 8 hours in a $FeCl_3$ solution. Then, the PR/Gr was rinsed with DI water to remove $FeCl_3$ residues and waited for another half hour in hydrochloric acid (HCl). After the sample was removed from HCl it is rinsed with DI water and dried with N_2, PR/Gr became ready to be transferred onto the SiO_2/n-Si substrate. The PR/Gr/substrate was placed on the hot plate at 100 °C for 6 min to adhere the PR on the substrate surface. Finally, to obtain graphene on the substrate, the PR/Gr/substrate was rinsed twice with acetone (7 min), IPA (7 min), and DI water (5 min) to remove PR. Finally, the resistance of the formed Gr/SiO_2/n-Si substrate was checked.

2.5. Lab-Built Cu Wire Bonder System

After transferring Gr onto the n-Si, the number of Gr layers is determined by Raman spectroscopy measurements. Electrical contacts are done to perform electronic and

optoelectronic measurements. The devices, which were pasted to the printed circuit board (PBC) with double-sided tape, were soldered using the wire bonding system in our laboratory, shown in Figure 2.8. The Cu paths on the PCB were soldered with 6-pin sockets to connect to the measurement set. Then, 80 mm of Cu wires were soldered between the Au contacts of the devices and the Cu paths of the PCB. Here, indium wire at 200 ^{o}C was used as the soldering material for the Au contacts on the device. Thanks to the low temperature melting property of indium, the connection is made to the pins of the PBC without damaging the contacts. Finally, both solder connections and the resistance of the device were checked with a Fluke 28-II TRMS Industrial Multimeter.

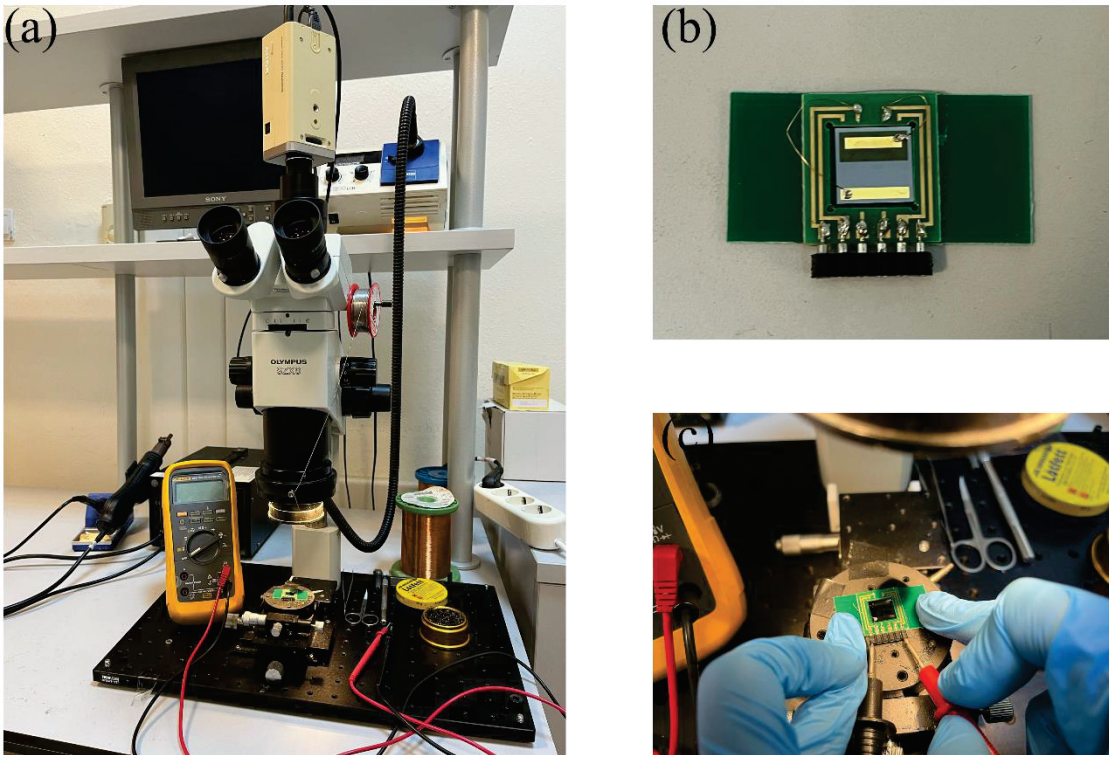

Figure 2.8. Lab-built wire bonding system including Sony ExwaveHAD Color Video Camera, Olympus U-CMAD3 Camera Adapter, Olympus U CMAD3/UTVIX- 2 Mount Microscope Camera Adapter, Olympus WHS10X-H/22 Microscope Eye Piece, Olympus SZX9 Stereo Zoom Microscope, Sunline 852D+SMD Rework Station, Emsan Enamelled Insulated Copper wire, and Zeiss KL 1500 LCD Cold Light Source, and Fluke 28-II TRMS Industrial Multimeter with IP67 Rating. (b) Our fabricated photodetector (c) Measurement of our device with a Multimeter.

2.6. Electronic and Optoelectronic Characterization

To examine the electrical behaviour of the device, it is important to determine the current-voltage (I-V) characteristics under light and in dark conditions. The I-V measurements help to determine the resistance, threshold voltage and light sensitivity of the photodiode under light and dark. The optical behaviour of the photodiode under light of different wavelengths such as UV, visible and NIR allows for the characterization of the photocurrent response. Time-dependent photocurrent spectroscopy measurements are performed to measure the response speed of the photodiode to optical signals with a LED source.

The photocurrent measurements setup is shown in Figure 2.9. Electronic and optoelectronic characterizations were carried out by using the rack unit with necessary equipment including Keithley 2400 source-meter unit - Keithley 6220 Precision Current Source as voltage and current sources, Keithley 6485 Picoammeter - Keithley 2000 Digital Multimeter for delicate current and voltage measurements shown in Figure 2.9.(a). The measurements were done with a Xenon light source, a high-resolution monochromator (Newport, Oriel Cornerstone), and Oceans Optics UV-VIS-NIR spectrometer.

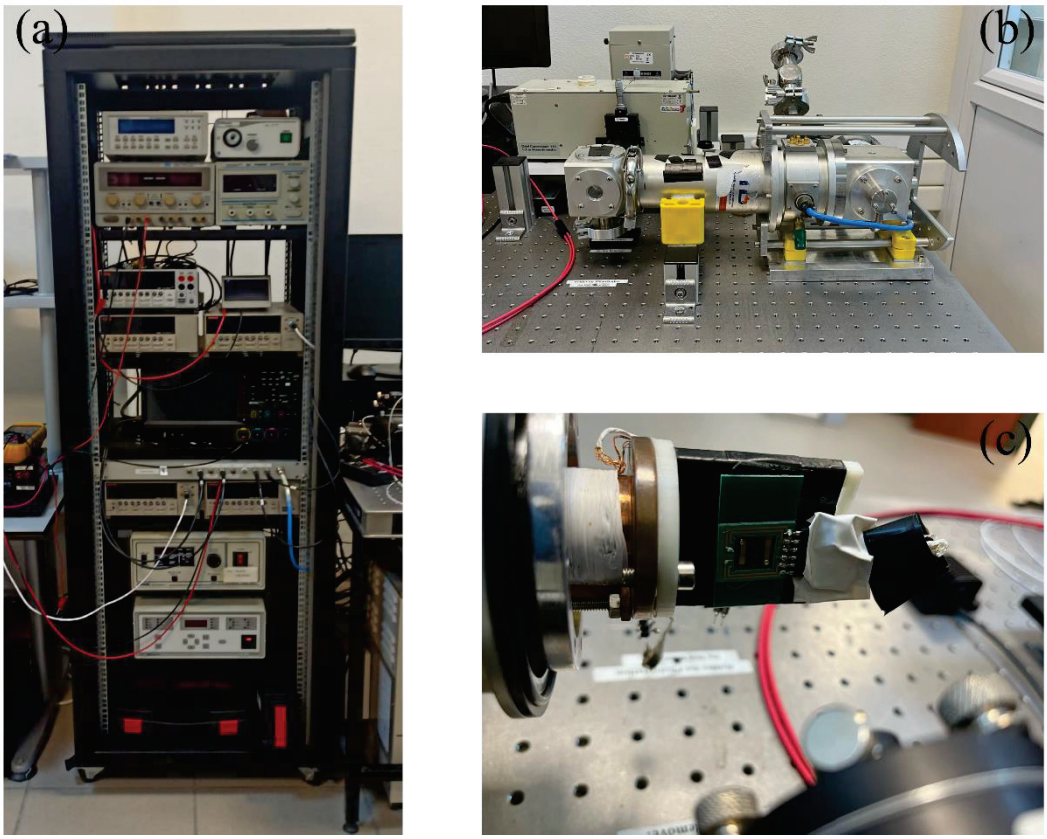

Figure 2.9. (a) The Electronic and Optoelectronic unit including Keithley 2400 Source meter Units, Keithley 6485 Picoammeter, Keithley 2182 Nanovoltmeter, Rigol MSO5204 Digital Oscilloscope, GW-Instek power supply, Orial Instruments 68831 300W Radiometric Power Supply, Thorlabs AMP102 Transimpedance Amplifier, Thorlabs DC2200 High Power LED Controller, and Thorlabs COP4-B Collimation Adapter (b) Photocurrent spectroscopy set-up including Xenon light source, Newport Focusing Assembly, Oriel Cornerstone high-resolution monochromator, Oceans Optics flame spectrometer (c) Fabricated Gr/Si photodiode placed onto cryostat's sample holder.

CHAPTER 3

RESULTS AND DISCUSSION

3.1. Raman Characterization

Raman spectroscopy measurements were done with a 532 nm wavelength laser source. As shown in Figure 3.1 (a) all the Raman spectra acquired on each sample exhibited graphene-related G and 2D signals at around 1582 cm^{-1} and 2700 cm^{-1}, respectively. The peak intensity ratio of I_{2D}/I_G for the sample with bilayer graphene was determined to be ~1 and for the samples with 4 or 6 layers of graphene electrode was found to be $I_{2D}/I_G < 1$. These obtained values are in good agreement with the ones given in the literature for CVD graphene (Malard et al. 2009).

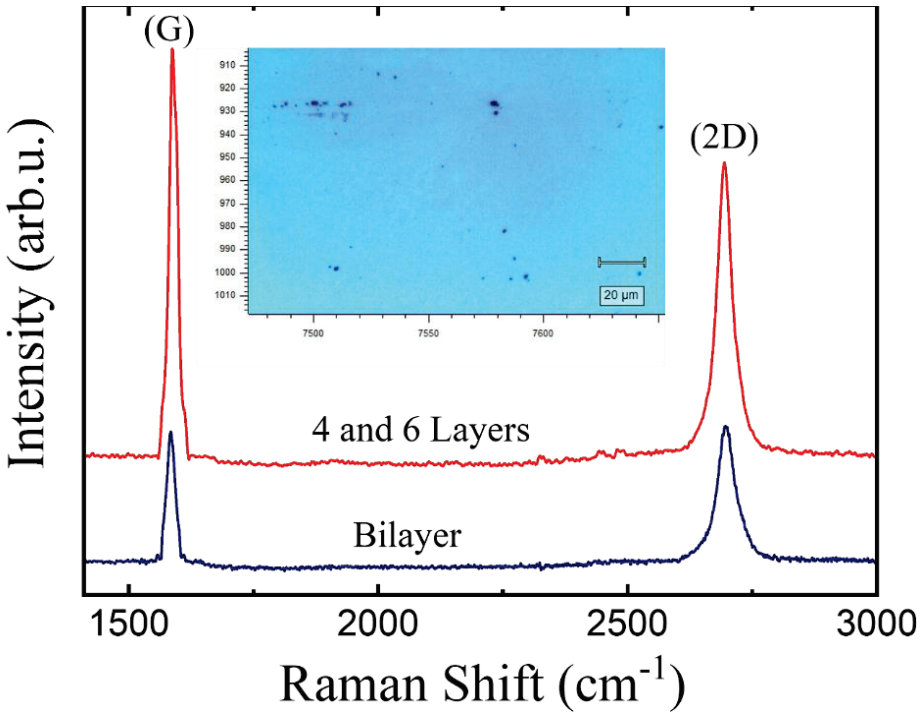

Figure 3.1. The Raman Spectrum peaks were taken from different spots and randomly chosen areas for the 2 layers, 4 layers, and 6 layers graphene on n-Si. Inset is a micro-Raman microscope image from the chosen areas of the 2-, 4 and 6-layer graphene electrode on n-Si.

3.2. Electronic Characterizations of Gr/Si-based Schottky Photodiode

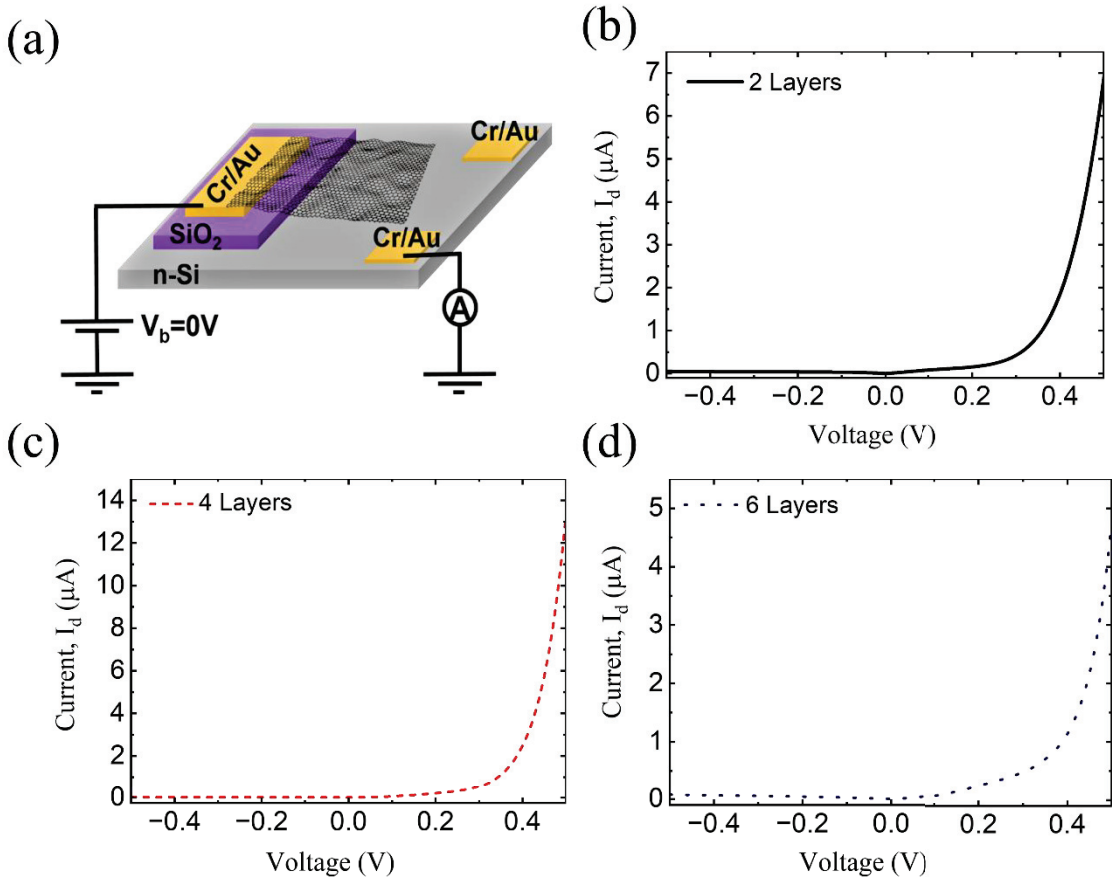

Figure 3.2. (a) Illustration of the Gr/Si- based Schottky photodiode, and (b) I-V measurements of devices with 2-, 4- and 6-layers graphene electrode.

I-V measurements are very important experimental methods for determining the electronic properties of the photodiodes (Zeghdar et al. 2015; Y. Kim et al. 2016). A typical device structure of Gr/Si-based Schottky photodiode is given in Figure 3.2 (a). We carried out I-V measurements on three different devices with 2, 4 and 6 layers of graphene electrodes. For an applied bias voltage range between -0.5 to 0.5 V at the room temperature, the results were plotted in Figure 3.2. (b), (c), and (d). As revealed by the I-V measurements taken under dark conditions, all the samples exhibited Schottky junction rectification character. All devices exhibit Schottky junction rectification character with an asymmetric and nonlinear current variation at the reverse and forward bias regions as seen in the Figure 3.3 (a). We found that the reverse saturation currents (I_0) are different

for the samples with 2, 4 and 6 layers of graphene electrodes. The dark currents (I_d) at zero-bias were determined to be ~ 0.56 nA for all the samples.

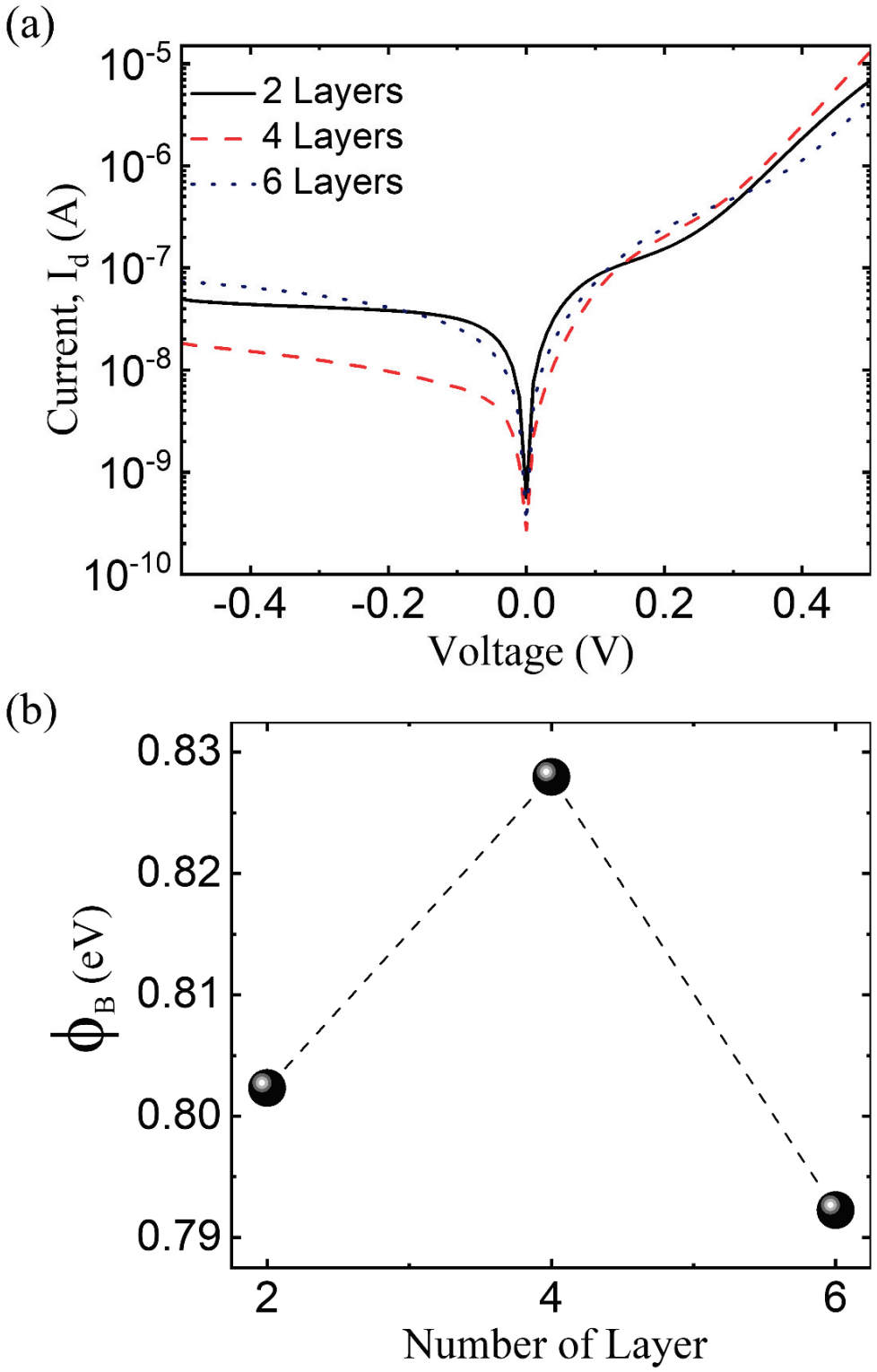

Figure 3.3. (a) Semi-logarithmic scale I-V curves of the photodetector with 2 layers of graphene electrode, 4 layers of graphene electrode, and 6 layers of graphene electrode and (b) Schottky Barrier Height in Gr/Si Schottky devices as a function of number of graphene layer.

The I–V characteristics of Gr/Si-based Schottky photodiode can be analysed by the thermionic emission (TE) model given below; (Cheung and Cheung 1986; Di Bartolomeo et al. 2018)

$$I = I_0 \left[exp\left(\frac{qV}{\eta k_B T}\right)\right] - 1 \qquad (3.1)$$

where η is the ideality factor and I_0 is the reverse saturation current which can be written as (H. Y. Kim et al. 2013),

$$I_0 = AA^* T^2 \exp(-\frac{q\Phi_B}{k_B T}) \qquad (3.2)$$

Equation 3.2 can be arranged to determine the Schottky barrier heights (Φ_B) as in the following:

$$\Phi_B = -\frac{k_B T}{q} ln\left(\frac{I_0}{AA^* T^2}\right) \qquad (3.3)$$

where k_B is the Boltzmann constant, T is the temperature (300 K), q is the elementary charge (1.661×10^{-19} C), A is the junction area (15 mm^2 for all our devices), A^* is the effective Richardson constant for n-type Si wafer (112 A/cm^2K^2). Considering the I_0 values extracted from the I-V plot we calculated the Φ_B of the samples with 2-, 4- and 6-layers graphene electrodes. From the I-V data the I_0 values were determined to be 4.95 x 10^{-8} µA, 1.8 x 10^{-8} µA and 7.31 x 10^{-8} µA. The figure 3.4 shows the Φ_B of all our Gr/Si-based Schottky photodiodes. Φ_B is 0.80 eV, 0.82 eV and 0.79 eV for 2, 4 and 6 layers of the Gr/Si-based Schottky photodiode, respectively. The Φ_B was found to be increased to ~0.82 eV for 4 layers graphene electrode and then decreased to about ~0.79 eV for 6 layers graphene electrode. These obtained results suggest that the rectification strength in the Gr/Si photodiode can be modified with the number of graphene layers.

3.3. Optoelectronic Measurements of Gr/Si-based Schottky Photodiode

3.3.1. Transmission and Reflection Measurements

When light penetrates through graphene, some of the light is reflected from the substrate and some is absorbed. The optical reflection under 280 nm LED light for 2-, 4- and 6-layers graphene transferred on quartz is given in Figure 3.4 (a). Additionally, transmission measurements were carried out between the wavelength 250 and 400 nm with the same samples and the obtained results were shown in Figure 3.4 (b). These experimental results are important for determining the interaction of incident light with Gr/Si-based Schottky photodiode.

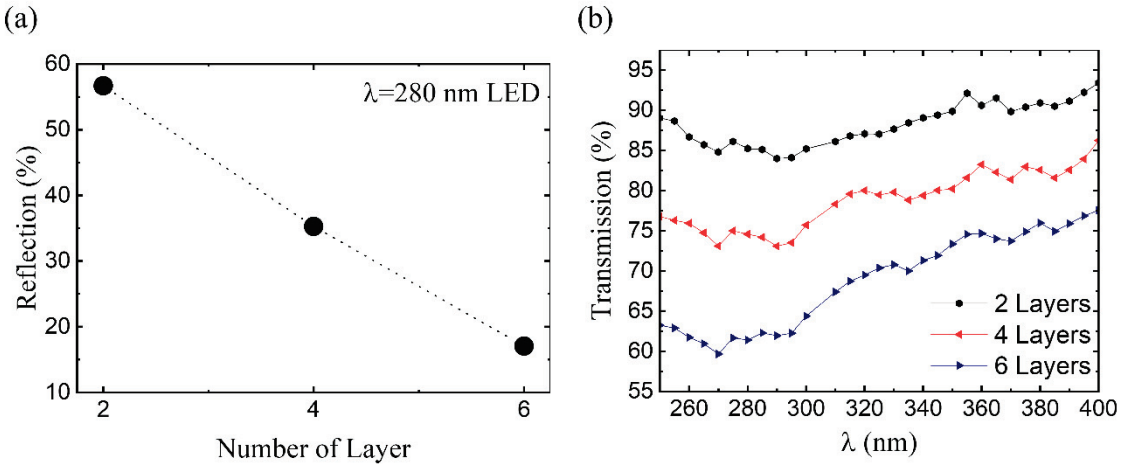

Figure 3.4: (a) Reflection data taken under 280 nm LED source illumination, and (b) Transmission data between the wavelength range 250 nm and 400 nm light expression as a percentage for 2-, 4- and 6-layers graphene samples.

3.3.2. Spectral Response Measurement

Spectral response (R) corresponds to the specific wavelength range light detection limit and the sensitivity capability of a photodiode (M. Fidan, O. Ünverdi, and C. Çelebi 2022; Lv et al. 2013). R can be calculated using the following equation:

$$R(\lambda) = \frac{I_p - I_d}{P(\lambda)} \qquad (3.4)$$

where the I_p is the photocurrent, I_d is the dark current and P (λ) is the incident light power at a certain wavelength. The R of all our devices was determined at zero bias (V_b = 0 V). To determine the R of devices in the UV region, we conducted wavelength-resolved photocurrent spectroscopy measurements at the wavelength range between 250 – 400 nm.

The R values of the samples are plotted in Figure 3.5. Independent of the number of graphene layers all the R data exhibit similar behaviour with almost a linear increment below the wavelength of 280 nm which is distinct from the spectral response of a typical p-n and p-i-n junction Si photodiode (Xu et al. 2016). Compared to the one for the device with 2 layers graphene electrode R increases by a factor of 3 for the device with 4 layers of graphene electrode. However, in the case of the device with 6 layers of graphene electrode R decreases about 25% relative to the R of the device with 4 layers of graphene electrode.

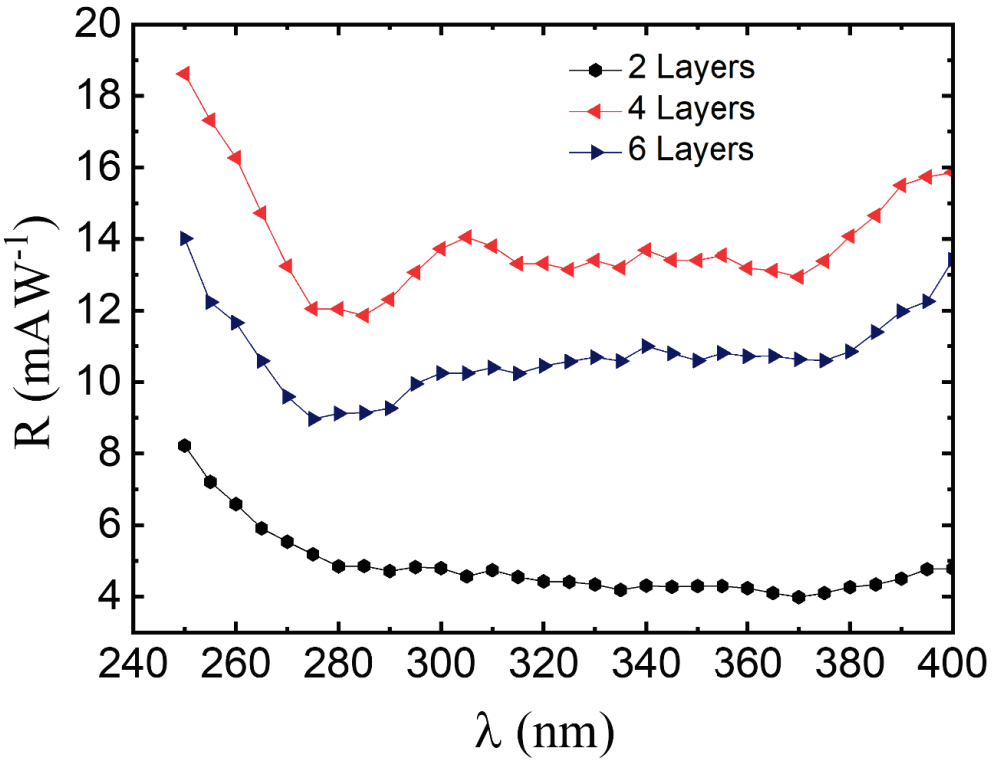

Figure 3.5. The spectral response measurements of Gr/Si- based Schottky photodiode with 2-, 4- and 6- graphene layers. The minimum spectral response was found at 280 nm for all devices.

The enhancement of the R in the deep-UV region below 280 nm for the G/n-Si Schottky barrier photodiode can be attributed to the presence of ultra-shallow junction at the G/Si interface along with high built-in potential promoting the separation of e-h pairs and suppressing the surface recombination (Wan et al. 2017).

The specific detectivity (D*) is a measure of the optimized sensitivity of the detector with respect to signal and background noise (Lv et al. 2013). In other words, D* is also defined as the ability to detect the weakest signal in the photodiode. D* can be written as:

$$D^* = \frac{A^{1/2}R(\lambda)}{\sqrt{2qI_d}} \qquad (3.5)$$

where A is the effective junction area (15 mm^2 for all our photodiodes), R(λ) is the spectral response at a specific wavelength (λ), q is the elementary charge, and I_d is the dark current.

Noise equivalent power (NEP) defines the incident power required to achieve a signal-to-noise ratio of 1 for a 1 Hz bandwidth. NEP is the detection ability of a photodetector, and the given as:

$$NEP = \frac{A^{1/2}}{D^*} \qquad (3.5)$$

Figure 3.6 displays D* and NEP results for Gr/Si-based Schottky photodiodes with 2-, 4- and 6-layers graphene electrode. We also determined D* of all devices produced by extracting the data from the R curves, as expressed in equation 3.3. D* for all devices behaves similarly to R at the wavelength range between 250 – 400 nm. Compared with the device with 2 layers graphene electrode, D* increases by 3 times in the device with 4 layers graphene electrode. Nevertheless, in the device with 6 layers graphene electrode, D* decreases by approximately 25% compared to the D* of the device with 4 layers graphene electrode. NEP results for all devices behave the same with D* in the 250 – 400 nm wavelength range. Compared with the device with 2 layers graphene electrode, NEP increases almost 3 times in the device with 4 layers graphene electrode. On the other hand, in the device with 6 layers graphene electrode, NEP decreases by approximately 25% compared to the NEP of the device with 4 layers graphene electrode. In Figure 3.6 (a), light signal detection capacity for all devices is low at 280 nm. As seen in Figure 3.6. (b) the noise power for all devices is maximum at 280 nm.

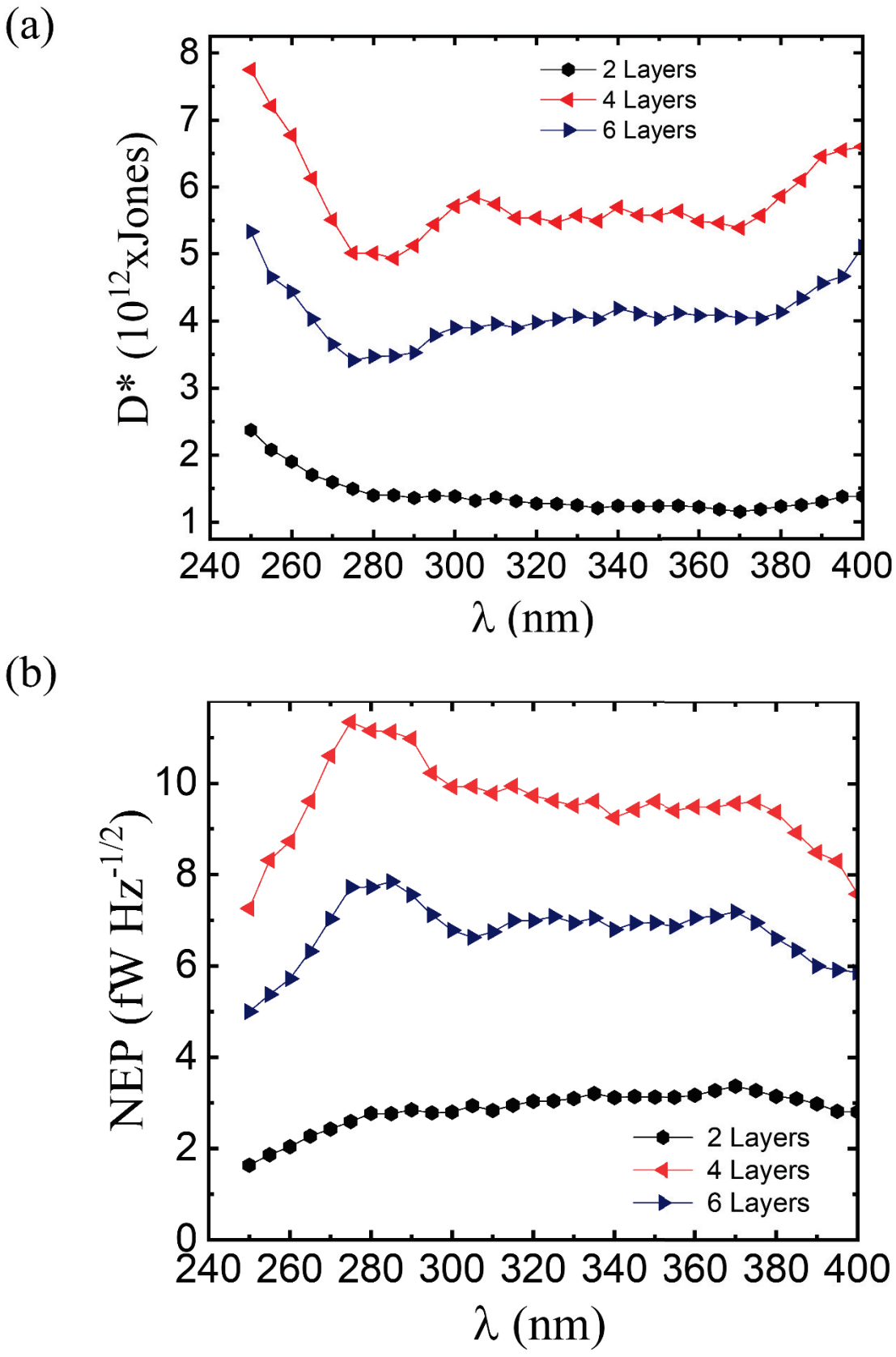

Figure 3.6. (a) D* and (b) NEP curves of our Gr/Si Schottky photodiode as a function of wavelength

3.3.3. Time-Dependent Photocurrent Spectroscopy Measurements

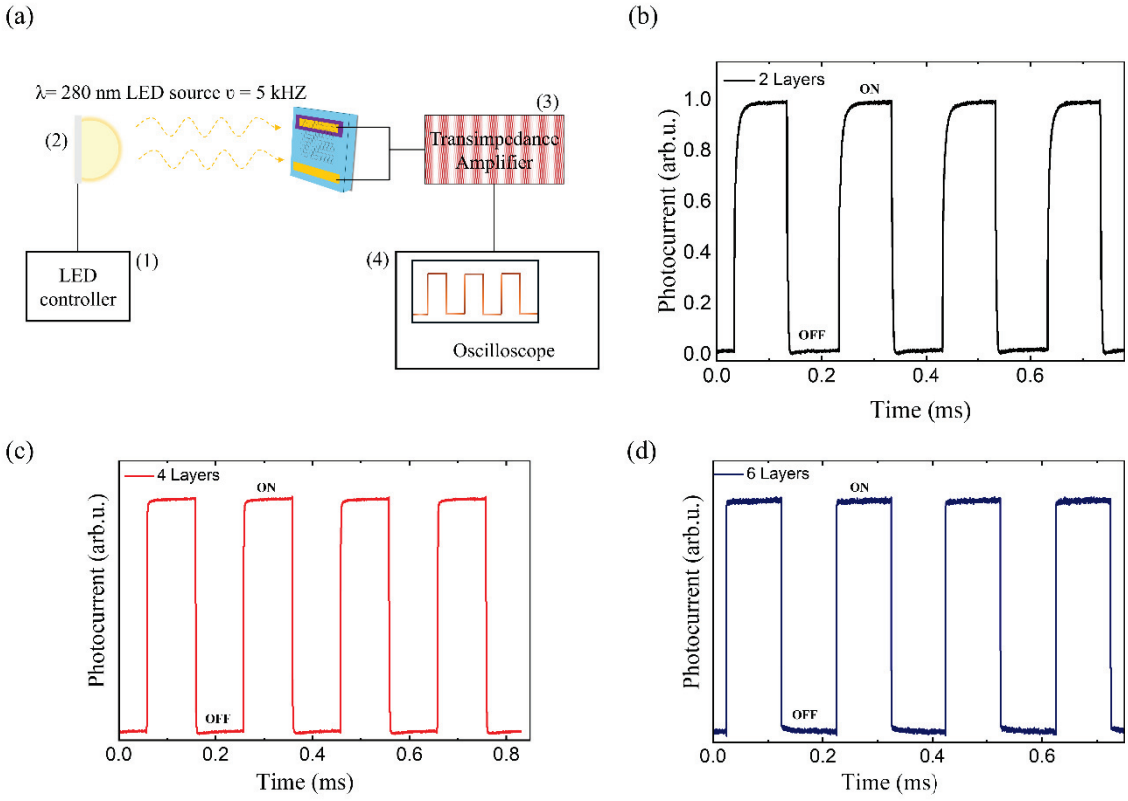

Figure 3.7. Time-dependent transient photocurrent measurements for Gr/Si Schottky photodiodes with (a) the experimental setup (b) 2 layers graphene electrode, (b) 4 layers graphene electrode and (d) 6 layers graphene electrode.

Time- dependent photocurrent measurements were carried out over several on/off switching under 280 nm LED light source illumination at a 5 kHz pulse frequency. Time-dependent photogenerated current at large periods by on/off measurements is shown in Figure 3.7 (b), (c), and (d) for Gr/Si Schottky devices with 2-, 4-, and 6-layers graphene electrode, respectively. When the light penetrates Gr/Si interface, electron-hole pairs are formed by photoexcitation. As a result, the electrons and holes are accelerated in the opposite direction due to the internal electric field, and hence photocurrent is created. Single period measurements were detected reaction to the light signal of all devices. Rise time (t_r) is defined as the photocurrent rising between the range of 10 and 90% of the maximum value of normalized photocurrent (Xinming Li et al. 2016). Further, fall time (t_f) is defined in a similar calculation method. The normalized-time-dependent photo-

response can be seen in Fig 3.8 (a) of 2 layers graphene electrode, (b) of 4 layers graphene electrode and (c) of 6 layers graphene electrode. The t_r of our samples are determined to be 0.2 µs, 0.11 µs and 0.14 µs, respectively. In addition, t_f is found to be 0.38 µs, 0.2 µs and 0.26 µs, respectively. The measurements showed that the response speed of the device with 4 layers graphene electrode is the highest among all other samples.

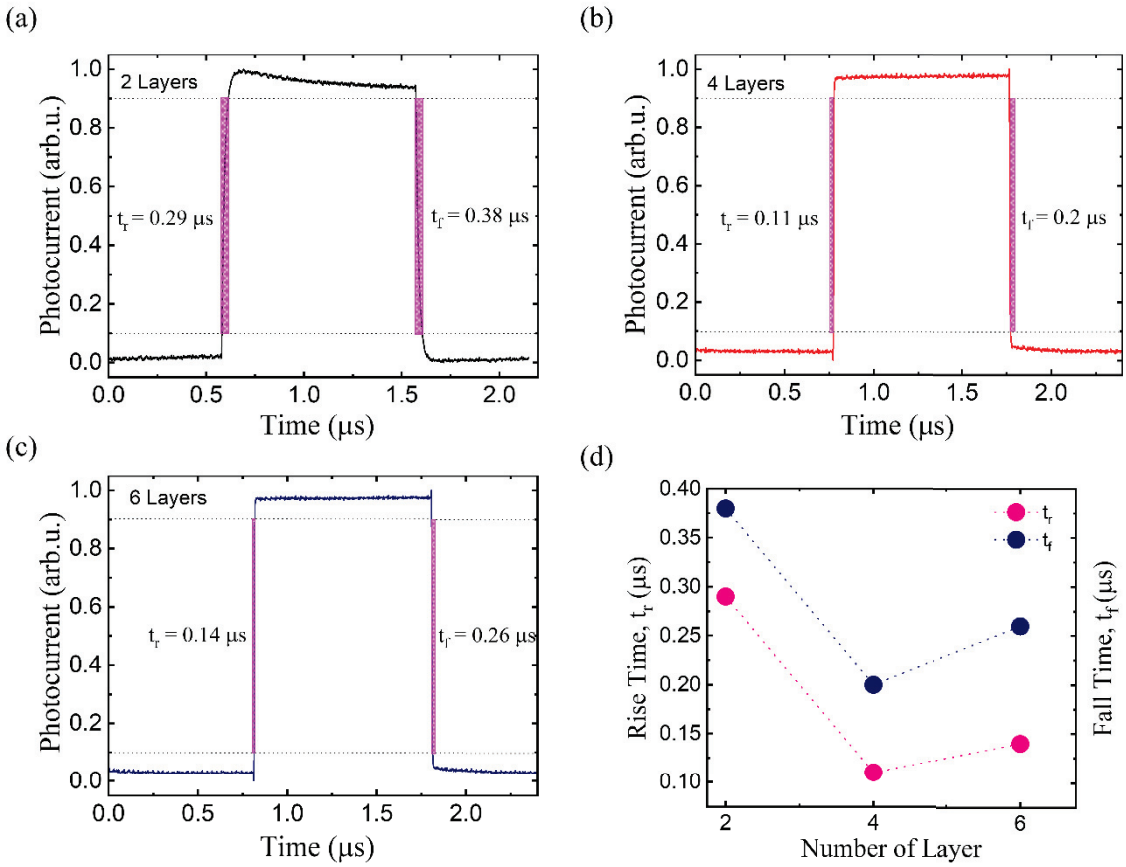

Figure 3.8. One cycle time-resolved photocurrent spectrum of Gr/Si photodiodes with (a) 2 layers, (b) 4 layers, (c) 6 layers graphene electrode, and (d) change graph depending on the number of layers. The measurements were done at $V_b = 0$ V under 280 nm wavelength UV light pulse.

3.4. Photocurrent Generation in Gr/Si Schottky Barrier Photodiode Under UV Light Illumination

The schematic illustration in Figure 3.9 is the energy band diagram of the Gr/Si-based Schottky junction photodiode under UV light illumination. In the first case, when Si and Gr get in contact that is a difference in the Schottky junction of the Fermi levels. The electrons in the Si are injected into the Gr until thermal equilibrium is achieved to balance the Fermi levels at the Gr electrode. Then photons pass through Gr electrode, between active area in the Gr/Si junction to create an electron-hole (e-h) pairs in the depletion region. Electrons are moved to Si and holes moved toward the Gr electrode, give rise to a measurable photocurrent in the device (M. Fidan et al. 2022; Pelella et al. 2021).

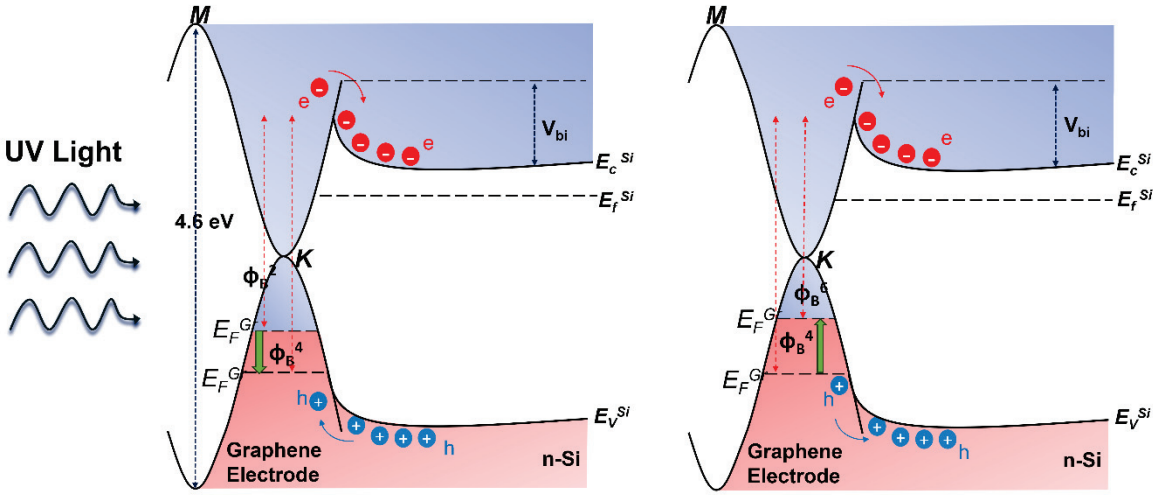

Figure 3.9. Schematic illustration of the energy band diagram for the Gr/Si Schottky heterojunction under the UV light. It represents the differences in Fermi levels, SBH and electron or hole transitions between (a) 2-layers graphene electrode and 4-layers graphene electron (b) 4-layers graphene electrode and 6-layers graphene electrode.

Increasing the number of graphene layers transferred onto Si increases the hole density and therefore the Fermi level shifts to a high energy state compared to the case in the thermal equilibrium. At the Gr/Si interface, the shift of graphene's Fermi level

changes the magnitude of ϕ_B (M. Fidan et al. 2022). In the scheme seen in Figure 3.9 (a), due to the Fermi level of the 4 layers graphene electrode (E_f^4) is lower, the ϕ_B is also expected to be large as a result of the built-in potential increases (Di Bartolomeo 2016; Wan et al. 2017).

In Figure 3.9 (b), the Fermi level of the 6 layers graphene electrode (E_f^6) and the Si valance band are aligned. Due to the high hole density in the 6-layer graphene electrode, the holes are injected into Si. In this case, both electron and hole transfer occur from Gr to Si and the TE model becomes ineffective. Holes make a source gain mechanism because of the charge accumulation and image force lowering at the interface (Burm and Eastman 1996). As the hole injection into Si continues, the electron density of the 6 layers graphene electrode begins to increase. As a result, E_f^6 begins to shift upper level. An increase in the Fermi level causes a decrease in ϕ_B.

CONCLUSION

In this thesis work, we fabricated Gr/Si-based Schottky photodiodes with different number of graphene layer electrode and investigated the effect of the number of graphene layers on the spectral response in the UV region. Prior to the electronic characterizations of the fabricated devices, Raman spectroscopy measurements were conducted to verify the number of graphene electrodes transferred on Si substrate. Following detailed Raman analysis, we carried out I-V measurements on the devices for an applied bias voltage range between -0.5 to 0.5 V. As revealed by I-V measurements taken under dark conditions, all the samples exhibited asymmetric I-V curves and Schottky junction rectification characteristics in the reverse and forward bias regions. We found that the reverse saturation currents are different for the samples with 2-, 4- and 6-layers graphene electrodes such as 4.95×10^{-8} nA, 1.93×10^{-8} nA and 7.3×10^{-8} nA, respectively. The dark currents at zero-bias were measured to be 5.6×10^{-10} μA, 2.7×10^{-10} μA and 5.6×10^{-10} μA. Φ_B were calculated using the TE model and we found 0.80 eV, 0.82 eV and 0.79 eV, respectively, for the 2-, 4- and 6-layers graphene electrode. These results show that the rectification strength can be changed by the number of graphene layers acting as transparent conductive electrodes in the device structure.

To determine the R of devices in the UV region, we performed photocurrent spectroscopy measurements at the wavelength range of 250 – 400 nm. The minimum spectral response was found at 280 nm for all devices. Also, the sensitivity of the device with a 4-layers graphene electrode increases by 3 times compared to that of a 2-layers graphene electrode. However, we observed 6 layers graphene electrode decrease by approximately 25% compared to the 4 layers graphene electrode of R values. For all devices, D* and NEP behave similarly to R in the wavelength range of 250 – 400 nm. The tr of the samples are founded to be 0.2 μs, 0.11 μs and 0.14 μs, and t_f is 0.38 μs, 0.2 μs and 0.26 μs, respectively, for 2-, 4- and 6-layers graphene electrode.

In conclusion, optoelectronic measurements showed that the TE model is effective for 2-layers graphene electrode and 4-layers graphene electrode. The charge accumulation and image-force lowering between the Si interface with the 6-layers graphene electrode caused the hole transition and E_f^6 to shift to upper levels. The experiments revealed that 4-layers graphene electrode showed the best performance. This work shows that the 4-

layers graphene electrode should be considered the upper limit for Si/Gr barrier photodiodes for UV light detection applications.

REFERENCES

Allen, Matthew J., Vincent C. Tung, and Richard B. Kaner. 2010. "Honeycomb Carbon: A Review of Graphene." *Chemical Reviews* 110 (1). https://doi.org/10.1021/cr900070d.

Andres, P. L. De, R. Ramírez, and J. A. Vergés. 2008. "Strong Covalent Bonding between Two Graphene Layers." *Physical Review B - Condensed Matter and Materials Physics* 77 (4). https://doi.org/10.1103/PhysRevB.77.045403.

Bartolomeo, Antonio Di. 2016. "Graphene Schottky Diodes: An Experimental Review of the Rectifying Graphene/Semiconductor Heterojunction." *Physics Reports*. https://doi.org/10.1016/j.physrep.2015.10.003.

Bartolomeo, Antonio Di. 2020. "Emerging 2d Materials and Their van Der Waals Heterostructures." *Nanomaterials*. https://doi.org/10.3390/nano10030579.

Bartolomeo, Antonio Di, Giuseppe Luongo, Laura Iemmo, Francesca Urban, and Filippo Giubileo. 2018. "Graphene-Silicon Schottky Diodes for Photodetection." *IEEE Transactions on Nanotechnology* 17 (6). https://doi.org/10.1109/TNANO.2018.2853798.

Bashir, Almas, Tahir Iqbal Awan, Aqsa Tehseen, Muhammad Bilal Tahir, and Mohsin Ijaz. 2020. "Interfaces and Surfaces." *Chemistry of Nanomaterials: Fundamentals and Applications*, January, 51–87. https://doi.org/10.1016/B978-0-12-818908-5.00003-2.

Bonaccorso, F., Z. Sun, T. Hasan, and A. C. Ferrari. 2010. "Graphene Photonics and Optoelectronics." *Nature Photonics* 4 (9). https://doi.org/10.1038/nphoton.2010.186.

Burm, Jinwook, and Lester F. Eastman. 1996. “Low-Frequency Gain in MSM Photodiodes Due to Charge Accumulation and Image Force Lowering.” *IEEE Photonics Technology Letters* 8 (1). https://doi.org/10.1109/68.475796.

Castro Neto, A. H., F. Guinea, N. M.R. Peres, K. S. Novoselov, and A. K. Geim. 2009. “The Electronic Properties of Graphene.” *Reviews of Modern Physics* 81 (1). https://doi.org/10.1103/RevModPhys.81.109.

Cheung, S. K., and N. W. Cheung. 1986. “Extraction of Schottky Diode Parameters from Forward Current-Voltage Characteristics.” *Applied Physics Letters* 49 (2). https://doi.org/10.1063/1.97359.

Dash, G. N., Satya R. Pattanaik, and Sriyanka Behera. 2014. “Graphene for Electron Devices: The Panorama of a Decade.” *IEEE Journal of the Electron Devices Society* 2 (5). https://doi.org/10.1109/JEDS.2014.2328032.

Fates, Rachid, Hachemi Bouridah, and Jean Pierre Raskin. 2019. “Probing Carrier Concentration in Gated Single, Bi- and Tri-Layer CVD Graphene Using Raman Spectroscopy.” *Carbon* 149. https://doi.org/10.1016/j.carbon.2019.04.078.

Ferrari, A. C., J. C. Meyer, V. Scardaci, C. Casiraghi, M. Lazzeri, F. Mauri, S. Piscanec, et al. 2006. “Raman Spectrum of Graphene and Graphene Layers.” *Physical Review Letters* 97 (18). https://doi.org/10.1103/PhysRevLett.97.187401.

Fidan, M., G. Dönmez, A. Yanilmaz, Ünverdi, and C. Çelebi. 2022. “Light-Induced Modification of the Schottky Barrier Height in Graphene/Si Based near-Infrared Photodiodes.” *Infrared Physics and Technology* 123. https://doi.org/10.1016/j.infrared.2022.104165.

Fidan, Mehmet, Özhan Ünverdi, and Cem Çelebi. 2022. “Enhancing the Photo-Response Characteristics of Graphene/n-Si Based Schottky Barrier Photodiodes by Increasing the Number of Graphene Layers.” *Journal of Vacuum Science & Technology A* 40 (3). https://doi.org/10.1116/6.0001758.

Geim, A. K., and K. S. Novoselov. 2007. “The Rise of Graphene.” *Nature Materials* 6 (3). https://doi.org/10.1038/nmat1849.

Giubileo, Filippo, and Antonio Di Bartolomeo. 2017. “The Role of Contact Resistance in Graphene Field-Effect Devices.” *Progress in Surface Science*. https://doi.org/10.1016/j.progsurf.2017.05.002.

Gupta, Ankur, Tamilselvan Sakthivel, and Sudipta Seal. 2015. “Recent Development in 2D Materials beyond Graphene.” *Progress in Materials Science*. https://doi.org/10.1016/j.pmatsci.2015.02.002.

Jehad, Ala K., Mehmet Fidan, Özhan Ünverdi, and Cem Çelebi. 2023. “CVD Graphene/SiC UV Photodetector with Enhanced Spectral Responsivity and Response Speed.” *Sensors and Actuators A: Physical* 355. https://doi.org/10.1016/j.sna.2023.114309.

Kim, Hye Young, Kangho Lee, Niall McEvoy, Chanyoung Yim, and Georg S. Duesberg. 2013. “Chemically Modulated Graphene Diodes.” *Nano Letters* 13 (5). https://doi.org/10.1021/nl400674k.

Kim, Yonghun, Ah Ra Kim, Jin Ho Yang, Kyoung Eun Chang, Jung Dae Kwon, Sun Young Choi, Jucheol Park, et al. 2016. “Alloyed 2D Metal-Semiconductor Heterojunctions: Origin of Interface States Reduction and Schottky Barrier Lowering.” *Nano Letters* 16 (9). https://doi.org/10.1021/acs.nanolett.6b02893.

Li, Sheng S. 1993. *Semiconductor Physical Electronics*. *Semiconductor Physical Electronics*. https://doi.org/10.1007/978-1-4613-0489-0.

Li, Xinming, Miao Zhu, Mingde Du, Zheng Lv, Li Zhang, Yuanchang Li, Yao Yang, et al. 2016. “High Detectivity Graphene-Silicon Heterojunction Photodetector.” *Small* 12 (5). https://doi.org/10.1002/smll.201502336.

Li, Xuesong, Weiwei Cai, Jinho An, Seyoung Kim, Junghyo Nah, Dongxing Yang, Richard Piner, et al. 2009. “Large-Area Synthesis of High-Quality and Uniform Graphene Films on Copper Foils.” *Science* 324 (5932). https://doi.org/10.1126/science.1171245.

Lv, Peng, Xiujuan Zhang, Xiwei Zhang, Wei Deng, and Jiansheng Jie. 2013. “High-Sensitivity and Fast-Response Graphene/Crystalline Silicon Schottky Junction-Based near-IR Photodetectors.” *IEEE Electron Device Letters* 34 (10). https://doi.org/10.1109/LED.2013.2275169.

Malard, L. M., M. A. Pimenta, G. Dresselhaus, and M. S. Dresselhaus. 2009. “Raman Spectroscopy in Graphene.” *Physics Reports*. https://doi.org/10.1016/j.physrep.2009.02.003.

Marconcini, P., and M. Macucci. 2007. “A Novel Choice of the Graphene Unit Vectors, Useful in Zone-Folding Computations.” *Carbon* 45 (5). https://doi.org/10.1016/j.carbon.2006.12.020.

Morozov, S. V., K. S. Novoselov, M. I. Katsnelson, F. Schedin, D. C. Elias, J. A. Jaszczak, and A. K. Geim. 2008. “Giant Intrinsic Carrier Mobilities in Graphene and Its Bilayer.” *Physical Review Letters* 100 (1). https://doi.org/10.1103/PhysRevLett.100.016602.

Muñoz, Roberto, and Cristina Gómez-Aleixandre. 2013. “Review of CVD Synthesis of Graphene.” *Chemical Vapor Deposition*. https://doi.org/10.1002/cvde.201300051.

Nair, R. R., P. Blake, A. N. Grigorenko, K. S. Novoselov, T. J. Booth, T. Stauber, N. M.R. Peres, and A. K. Geim. 2008. “Fine Structure Constant Defines Visual Transparency of Graphene.” *Science* 320 (5881). https://doi.org/10.1126/science.1156965.

Novoselov, K. S., V. I. Fal’Ko, L. Colombo, P. R. Gellert, M. G. Schwab, and K. Kim. 2012. “A Roadmap for Graphene.” *Nature*. https://doi.org/10.1038/nature11458.

Novoselov, K. S., A. K. Geim, S. V. Morozov, D. Jiang, M. I. Katsnelson, I. V. Grigorieva, S. V. Dubonos, and A. A. Firsov. 2005. “Two-Dimensional Gas of Massless Dirac Fermions in Graphene.” *Nature* 438 (7065). https://doi.org/10.1038/nature04233.

Pang, Shuping, Yenny Hernandez, Xinliang Feng, and Klaus Müllen. 2011. “Graphene as Transparent Electrode Material for Organic Electronics.” *Advanced Materials* 23 (25). https://doi.org/10.1002/adma.201100304.

Pelella, Aniello, Alessandro Grillo, Enver Faella, Giuseppe Luongo, Mohammad Bagher Askari, and Antonio Di Bartolomeo. 2021. “Graphene-Silicon Device for Visible and Infrared Photodetection.” *ACS Applied Materials and Interfaces* 13 (40). https://doi.org/10.1021/acsami.1c12050.

Periyanagounder, Dharmaraj, Paulraj Gnanasekar, Purushothaman Varadhan, Jr Hau He, and Jeganathan Kulandaivel. 2018. “High Performance, Self-Powered Photodetectors Based on a Graphene/Silicon Schottky Junction Diode.” *Journal of Materials Chemistry C* 6 (35). https://doi.org/10.1039/c8tc02786b.

Ponraj, Joice Sophia, Zai Quan Xu, Sathish Chander Dhanabalan, Haoran Mu, Yusheng Wang, Jian Yuan, Pengfei Li, et al. 2016. “Photonics and Optoelectronics of Two-Dimensional Materials beyond Graphene.” *Nanotechnology* 27 (46). https://doi.org/10.1088/0957-4484/27/46/462001.

Raj, Anant, and Jacob Eapen. 2019. “Phonon Dispersion Using the Ratio of Zero-Time Correlations among Conjugate Variables: Computing Full Phonon Dispersion Surface of Graphene.” *Computer Physics Communications* 238. https://doi.org/10.1016/j.cpc.2018.12.008.

Reina, Alfonso, Hyungbin Son, Living Jiao, Ben Fan, Mildred S. Dresselhaus, Zhong Fan Liu, and Jing Kong. 2008. “Transferring and Identification of Single- and Few-Layer

Graphene on Arbitrary Substrates." *Journal of Physical Chemistry C* 112 (46). https://doi.org/10.1021/jp807380s.

Suk, Ji Won, Wi Hyoung Lee, Jongho Lee, Harry Chou, Richard D. Piner, Yufeng Hao, Deji Akinwande, and Rodney S. Ruoff. 2013. "Enhancement of the Electrical Properties of Graphene Grown by Chemical Vapor Deposition via Controlling the Effects of Polymer Residue." *Nano Letters* 13 (4). https://doi.org/10.1021/nl304420b.

Suzuki, Akira, Masashi Tanabe, and Shigeji Fujita. 2017. "Electronic Band Structure of Graphene Based on the Rectangular 4-Atom Unit Cell." *Journal of Modern Physics* 08 (04). https://doi.org/10.4236/jmp.2017.84041.

Tongay, S., T. Schumann, X. Miao, B. R. Appleton, and A. F. Hebard. 2011. "Tuning Schottky Diodes at the Many-Layer-Graphene/Semiconductor Interface by Doping." *Carbon* 49 (6). https://doi.org/10.1016/j.carbon.2011.01.029.

Wan, Xia, Yang Xu, Hongwei Guo, Khurram Shehzad, Ayaz Ali, Yuan Liu, Jianyi Yang, et al. 2017. "A Self-Powered High-Performance Graphene/Silicon Ultraviolet Photodetector with Ultra-Shallow Junction: Breaking the Limit of Silicon?" *Npj 2D Materials and Applications* 1 (1). https://doi.org/10.1038/s41699-017-0008-4.

Wang, Yiming, Shuming Yang, Dasaradha Rao Lambada, and Shareen Shafique. 2020. "A Graphene-Silicon Schottky Photodetector with Graphene Oxide Interlayer." *Sensors and Actuators, A: Physical* 314. https://doi.org/10.1016/j.sna.2020.112232.

Wright, A. R., Feng Liu, and C. Zhang. 2009. "The Effect of next Nearest Neighbor Coupling on the Optical Spectra in Bilayer Graphene." *Nanotechnology* 20 (40). https://doi.org/10.1088/0957-4484/20/40/405203.

Xu, Yang, Cheng Cheng, Sichao Du, Jianyi Yang, Bin Yu, Jack Luo, Wenyan Yin, et al. 2016. "Contacts between Two- and Three-Dimensional Materials: Ohmic, Schottky, and p-n Heterojunctions." *ACS Nano*. https://doi.org/10.1021/acsnano.6b01842.

Yang, Yinxiao, and Raghu Murali. 2011. “Binding Mechanisms of Molecular Oxygen and Moisture to Graphene.” *Applied Physics Letters* 98 (9). https://doi.org/10.1063/1.3562317.

Zeghdar, Kamal, Lakhdar Dehimi, Achour Saadoune, and Nouredine Sengouga. 2015. “Inhomogeneous Barrier Height Effect on the Current-Voltage Characteristics of an Au/n-InP Schottky Diode.” *Journal of Semiconductors* 36 (12). https://doi.org/10.1088/1674-4926/36/12/124002.

Zhang, Y. Y., C. M. Wang, Y. Cheng, and Y. Xiang. 2011. “Mechanical Properties of Bilayer Graphene Sheets Coupled by Sp3 Bonding.” *Carbon* 49 (13). https://doi.org/10.1016/j.carbon.2011.06.058.